Plate and Butt-Weld Stresses Beyond Elastic Limit, Material and Structural Modeling

V. Verderaime
*George C. Marshall Space Flight Center
Marshall Space Flight Center, Alabama*

ACKNOWLEDGMENTS

TABLE OF CONTENTS

LIST OF ILLUSTRATIONS

LIST OF TABLES

TECHNICAL PAPER

PLATE AND BUTT-WELD STRESSES BEYOND ELASTIC LIMIT, MATERIAL AND STRUCTURAL MODELING

I. INTRODUCTION

The solid rocket booster (SRB) aft skirt is a 2219-T87 aluminum, high performance structure that supports the entire shuttle vehicle through stacking operations into liftoff. Two flight copies were tested to revised operational loads, and both failed at the same weld location at considerably less load than the estimated ultimate. Monitoring gauges also indicated the failure strain to be much less than predicted. This modeling and test prediction breakdown provoked an effort to understand the related physics of stresses beyond the elastic limit.

What makes the inquiry of inelastic behavior so compelling is that all high performance structures must embody this phenomenon in the ultimate safety factor analyses. Forty percent of the aft skirt strength is sustained by material properties beyond the elastic limit, a region not too well understood.

To gain basic insights on inelastic structural behavior, an analytical modeling approach was developed which incorporates nonlinear material properties with familiar linear strength of materials method. Material properties through the inelastic range were modeled from uniaxial test data and were applied to analysis of rectangular bars and plates subjected to tension, bending, and combined loadings. Associated stress and strain equations were derived in sufficient detail for the collective understanding and benefit of all interfacing disciplines, especially design, stress, materials, and test.

The analytical method is applicable to most strength of materials problems and may be extended to some classical elasticity models. It should be especially applicable to combustion device structures and aeroheated zones, where high temperatures decrease the elastic limit while extending the inelastic range of materials.

Metallurgical discontinuity stresses resulting from dissimilarity of weld and parent material properties beyond the elastic region are included. A previous paper [1] explored this phenomenon and in this report is made consistent with the succeeding material and analytical modeling technique.

Of 24 structural failures in Marshall Space Flight Center (MSFC) programs, the average ultimate test loading fell 15 percent below the predicted safety factor [2]. It is hoped that this paper will help to better understand the inelastic failure of elementary structures through the analytical method, will provide a quick backup analysis for comparing with new and existing computational methods, will identify practical limitations, and will support safe design analyses and test data evaluations.

II. MATERIALS MODELING

Curve *OACE* of figure 1 typifies the stress-strain data obtainable from a uniaxial tensile test of a polycrystalline material. Points *A* and *E* are the elastic limit and the ultimate stress properties, respectively. Line *OA* is the elastic portion of the curve which depends on the resilience between molecules. Plastic flow is the permanent deformation caused from displacement of atoms, or molecules, to new crystal lattice sites. When the applied stress exceeds the elastic limit, elastic straining decreases while plastic flow rate increases. The ratio of elastic strain and plastic flow defines the slope, and their change rate characterizes the nonlinear property of curve *ACE* as it approaches full plastic state.

The area under the stress-strain curve *OACE* represents the total strain energy per unit volume of the material. When the material is stressed inelastically to point *A'* and relaxed, it relaxes elastically (same slope as *OA*) to a new origin point *O'* for total plastic strain of *O–O'*. The material takes on a permanent set, and the strain energy represented by the area *OACA'O'* is not recoverable. Consequently, the new stress-strain property is defined by *O'A'E*, and the elastic limit advances to point *A'*. The plastic slip along the crystal boundary is directional, which transforms the isotropic material to anisotropic in the next load cycle.

Current structural design practice is based on linear material properties in which the stress-strain relationship to ultimate is defined by the slope of line *OA* extended to point *B*. Point *B* is equal to the ultimate stress at point *E*. This assumption is rather conservative for local discontinuity stresses because it embraces a small fraction of the total strain energy available for the ultimate safety factor. When operational loads on inventory structures are projected to increase beyond original design loads, it is prudent to calculate a new safety factor using the total strain energy, in which the increased energy may be sufficient to establish that actual margins are still within specifications.

The success of a nonlinear determination depends on the accuracy of the finite element method (FEM) code and structural modeling, and on the understanding of results. Sometimes, stress results of local areas from large commercial codes are so intricate and the mechanics so obscured that a hand analysis is necessary to interpret the physics. Often, new codes and options are difficult to verify, and they succumb to cookbook application. When this happens, a backup hand analysis of basic structural elements for comparison and perception becomes essential, and its applicability depends on the simplicity and compatibility of inelastic material expressions.
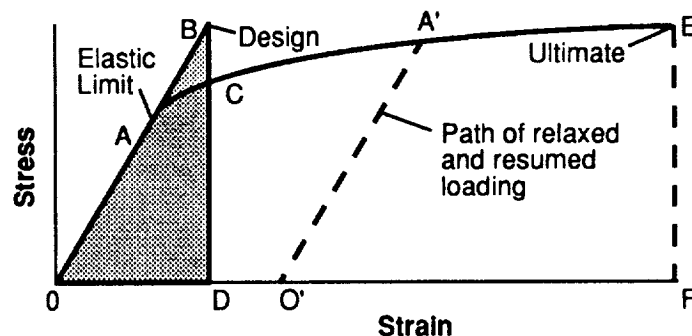

Figure 1. Design data from uniaxial test.

A. Uniaxial Stress-Strain

Uniaxial tension tests are the simplest type for obtaining mechanical properties of structural materials. Stress-strain material properties of commonly milled bars and plates are well defined and widely published [3], but properties of specially processed materials, such as welds, castings, and forging, are usually developed by the user. Such was the case of the SRB skirt butt-weld which is a good basis for this material modeling discussion. Properties defined and qualifications expressed are not standard, but may provide guidelines for designing material model tests applicable to analytical approaches.

Multipass butt-weld properties vary significantly with design geometry which influences the heat intensity and distribution across the weld and into adjacent heat affected zones (HAZ). Obviously, the stress-strain relationship across the weld width varies uniquely for each design and manufacturing process and must be obtained from sample test specimen. If properties of the HAZ are required and the width of the zone is less than the gauge length, similar properties in the adjacent overlapped zones must be determined and separated from the gauge data through the rule of mixtures. All this points to the difficulty of not only obtaining weld properties, but the necessity of discussing the data with the intended user.

The normal stress-strain test data for the SRB skirt analysis, presented in figure 2, was developed from 24 specimens [4], using 0.125-in electrical strain gauges mounted at midwidth on weld surfaces. The data is the statistical average of the sample size and is preferred for analytical methods that are to be used for tracking test instrumentation. Deviation of the data about the average is used to define the A-basis ultimate properties required for design analysis and test margin predictions.
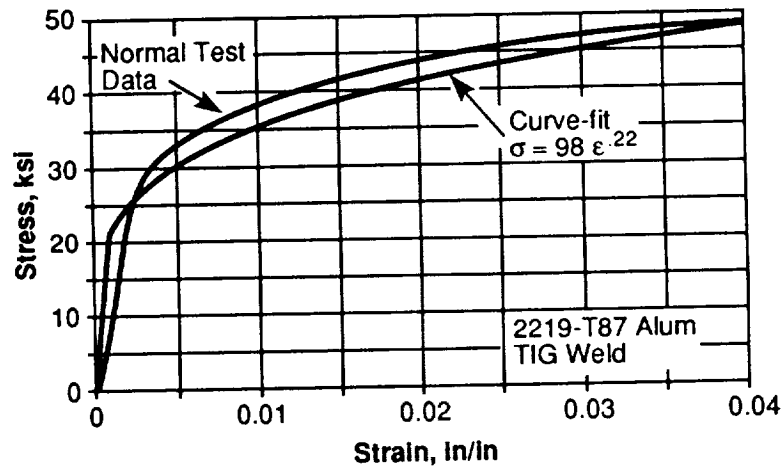

Figure 2. Curve-fit to weld test data.

Since stress is related to strain through material properties, and as stress increases beyond the elastic limit, these properties change nonlinearly with stress. The simplest normal stress-strain model representing these changes is a two-parameter curve-fit,

$$\sigma = a\varepsilon^b , \qquad (1)$$

where a is the strength coefficient and b is the strain hardening exponent. When $b = 1$, the expression reduces to Hooke's law of elasticity, and coefficient a is identically Young's modulus, E. When $b = 0$, pure plastic flow occurs at constant stress, and the material is said to be perfectly plastic (appendix C).

The two parameter model is particularly compatible with the analytical method because material properties expressed as coefficients and exponents of stress or strain are easily combined with stress and strain variables of strength formulas through their coefficients and exponents.

A conservative material representation should curve-fit the origin, elastic limit, and ultimate stress parameters without exceeding the area under the test data curve, as shown in figure 2. Data required to determine the two parameters of equation (1) are specified by properties at the two extreme conditions of the inelastic curve: Young's modulus, E; elastic limit stress, σ_{EL}; ultimate stress, σ_U; and ultimate strain, ε_U. The elastic limit stress, though difficult to isolate, is a more meaningful property in the inelastic process than the yield point. If maximum stress of very ductile materials precedes fracture, strains beyond maximum stress should be considered unstable, and the value at inception of maximum stress is assumed ultimate stress.

A better midrange curve-fit would be possible by using the true strain rather than the suggested engineering strain. However, the slight gain in accuracy would severely compromise the potential application of the analytical process. Besides, the error decreases as the stress approaches failure. Since proto-type test predictions require accurate midrange properties, a second set of materials models should be derived between the elastic limit to 20 percent beyond. At the same time, effects of maximum expected error should be weighed against effects of the coefficient-of-variation of material data which has been reported to exceed 20 percent [4].

The hardening exponent of equation (1) may be calculated from

$$b = \log(\sigma_U/\sigma_{EL})/\log(\varepsilon_U{}^*E/\sigma_{EL}) ,$$ (2)

and the coefficient from

$$a = \sigma_{EL}/(\sigma_{EL}/E)^b .$$ (3)

Subsequent material models derived from simple uniaxial tension data are expressed in stress or strain variables and cast in similar two-parameter form. This is a necessary condition for simplifying the analytical process.

An A-basis strength of material is defined as having a 99-percent reliability taken at a 95-percent confidence level. This tolerance limit is used for both elastic limit and ultimate strength. The A-basis strength is calculated from referenced weld test data having average strength of $\bar{\sigma}_U = 48.6$ ksi, standard deviation of $s = 1.6$ ksi, and a factor of $k = 3.18$ for a 24 sample size. Applying these values to the statistical criteria,

4

$$\sigma_U = \bar{\sigma} - ks , \tag{4}$$

results in a design ultimate stress of $\sigma_U = 43.5$ ksi. The A-basis elastic limit stress is $\sigma_{EL} = 20.5$ ksi. As the number of test specimen increases, the k-factor decreases to the limit of 2.33, which has trades implications as to the number of specimen required versus performance of the structure.

It must be pointed out that the material model specified above is compromised in three respects. First, equation (1) assumes a nonlinear stress-strain relationship throughout. This analytical method is definitely not applicable below the elastic limit, except as required to derive inelastic bending models. A more accurate relationship would have split the curve-fit into two parts; a standard linear part having $b = 1$ and $a = E$ up to the elastic limit of 26.3 ksi followed by the nonlinear part. However, incorporating this discontinuity in bending stress derivations would be extraneously complicated and will be shown to be insignificant beyond the elastic limit for which it is intended.

Secondly, the stress-strain curve of figure 2 assumes a symmetric material. There is reason to believe that most crystalline materials have different tension and compression elastic limits which may be demonstrated in a pure bending experiment. However, this is an order of refinement which is not necessary with current general developments.

Finally, it should be recognized that weld properties are not only manufacturing process dependent, but are also dependent on the mass distribution of the adjoining material along the weld length. If the weld is to join a highly sculptured forging, such as the skirt post, the heat sink will vary accordingly, as will the weld and the HAZ properties. Then the materials representation and number of models to be developed must be decided jointly by manufacturing and stress considerations. Does the weld thickness, therefore weld-heat, taper along the length? Does the maximum stress and weakest expected weld occur at independent places along the weld length, etc.? Similar questions may be asked of forgings and castings properties.

B. Poisson's Ratio

All polycrystalline materials possess two elastic constants from which all other constants may be derived. Young's modulus and Poisson's ratio may be obtained simultaneously from a simple uniaxial test specimen. Poisson's ratio is defined as the ratio of unit lateral contraction and unit axial extension, $\mu = -\varepsilon_y/\varepsilon_x = -\varepsilon_z/\varepsilon_x$, which suggests a volumetric relationship. When a material in uniaxial test is extended, the space between molecules in the crystal lattice are displaced linearly causing a minute volume increase. The new volume is related to the specimen dimensions and strains by

$$V = (L + L\varepsilon_x)(t + t\varepsilon_y)(B + B\varepsilon_z) .$$

Substituting Poisson's ratio expressions for lateral strains and ignoring high order terms, the volume change relates to Poisson's ratio by

$$\frac{\Delta V}{V} = (1 - 2\mu)\varepsilon_x .$$

In the elastic range, Poisson's ratio is a constant having a value between 0.28 to 0.33 for most common materials, and 0.3 is used in most general analyses. When a specimen is extended beyond the elastic limit, molecules that slip into new lattice sites cause no change in volume. Therefore, a totally plastic Poisson's ratio engages in no volume change and should not exceed $\mu_p = 0.5$. Consequently, as the axial strain increases beyond the elastic limit, the volume change rate decreases and Poisson's ratio approaches its maximum value.

Because the same molecular displacement process which occurs in the normal stress-strain relationship also is volume related, it would seem reasonable to expect Poisson's ratio to be expressed similarly to equation (1),

$$\mu = g\varepsilon_x^f .\tag{5}$$

Current practice is to express the Poisson's ratio nonlinearly with the secant modulus defined by normal stress-strain data. Using data developed in figure 2 and equation (1), Poisson's ratio based on secant modulus is

$$\mu = \mu_p - [\mu_A - \mu_e] \frac{\sigma}{E} \left[\frac{a}{\sigma}\right]^{1/b}\tag{6}$$

where subscripts p and e refer to plastic and elastic properties, respectively, and E is Young's modulus. This expression is adjusted to match the elastic Poisson's ratio with the elastic limit stress σ_{EL} through the variable μ_A given by,

$$\mu_A = \mu_p \frac{E}{\sigma_{EL}} \left[\frac{\sigma_{EL}}{a}\right]^{1/b} + \mu_e \left[1 - \frac{E}{\sigma_{EL}} \left[\frac{\sigma_{EL}}{a}\right]^{1/b}\right] .\tag{7}$$

Equation (6) is incompatible with the subsequent analytical method for reasons given in the above stress-strain expression. However, the secant model is still prerequisite to calculate the Poisson's ratios at the elastic limit stress μ_{EL} and at the ultimate stress μ_U. Using stresses from equation (1) and Poisson's ratio from equation (6), parameters of equation (5) are calculated similarly to the tension model:

$$f = \log[\mu_U/\mu_{EL}]/\log[\sigma_U/\sigma_{EL}]^{1/b} ,\tag{8}$$

$$g = \mu_{EL}/(\sigma_{EL}/a)^{f/b} .\tag{9}$$

6

Figure 3 presents the two constructed Poisson's ratio models discussed, based on uniaxial test data of figure 2. Though common end conditions were imposed on both models, a deviation of up to 10 percent is noted at midrange between the two plots. This deviation may affect monitoring and evaluating strain gauges on prototype structures. How much uncertainty is tolerated may be determined from sensitivity analyses of specific structural environments. Poisson's ratio expressed by equation (5) is more linearly related to stress and provides another option to correlate with actual test data.
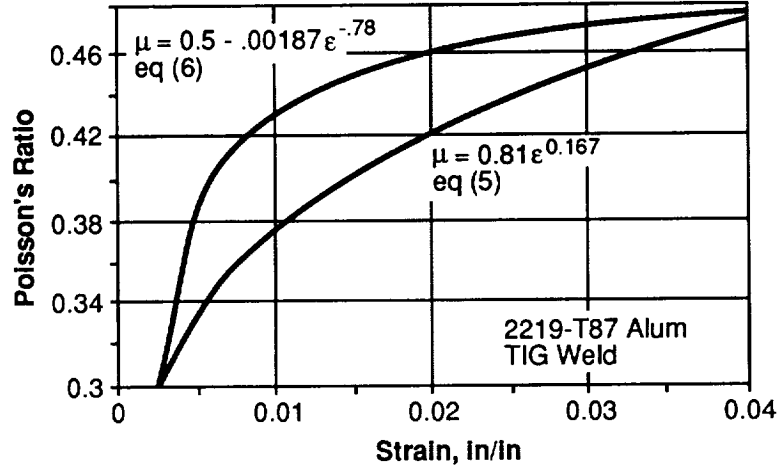
Figure 3. Constructed Poisson's ratio versus strain.

C. Failure Criteria

The total strain energy produced in multistress fields consists of energy causing a volume change and energy causing distortion. Basis for the failure theory is that distortion energy is limited and that hydrostatic strain does not cause failure. Therefore, hydrostatic strain is deleted from the total strain energy [5]. The distortion energy theory of failure hypothesizes that a material will fail when the energy of distortion of combined stresses achieves the same energy for failure in simple tension.

Using a two-dimensional stress field, the failure criterion is expressed by

$$\sigma_U^2 \leq \sigma_1^2 + \sigma_2^2 - \sigma_1 \sigma_2 \ , \tag{10}$$

where subscripts 1 and 2 refer to principal stresses. Roots of the characteristic equation formed from the two-dimensional stress tensor,

$$\begin{vmatrix} (\sigma_{xx} - \lambda) & \tau_{xz} \\ \tau_{xz} & (\sigma_{zz} - \lambda) \end{vmatrix} = 0 \ ,$$

define the inplane principal stresses,

7

$$\sigma_{1,2} = \frac{\sigma_x + \sigma_z}{2} \pm \frac{1}{2} \sqrt{(\sigma_x + \sigma_z)^2 - 4(\sigma_x \sigma_z - \tau_{xz}^2)} \ .$$

Substituting these roots into equation (10) gives the biaxial stress failure condition,

$$\sigma_U \leqslant \sqrt{\sigma_x^2 + \sigma_z^2 - \sigma_x \sigma_z + 3 \ \tau_{xz}^2} \ . \tag{11}$$

Shear stress is noted by τ, and σ_U is the maximum stress obtained from a uniaxial tension test. Note that when biaxial normal stresses have unlike polarity, the induced distortion energy to failure increases. When stresses have the same polarity, distortion energy decreases and is a capital benefit in pressure vessel designs.

The three-dimensional failure criteria is

$$\sigma_U^2 \leqslant \sigma_1^2 + \sigma_2^2 + \sigma_3^2 - \sigma_1 \sigma_2 - \sigma_1 \sigma_3 - \sigma_2 \sigma_3 \ , \tag{12}$$

and

$$\sigma_U \leqslant \sqrt{\sigma_x^2 + \sigma_y^2 + \sigma_z^2 - \sigma_x \sigma_y - \sigma_x \sigma_z - \sigma_y \sigma_z + 3 \ (\tau_{xy}^2 + \tau_{xz}^2 + \tau_{yz}^2)} \ . \tag{13}$$

Of the total strain energy under the stress-strain curve of figure 1, the elastic strain energy component, represented by the triangle OBD, provides the static strength of the material. What makes the total strain energy important in the ultimate safety factor analysis is that local structural regions, having stress concentrations exceeding the elastic limit, will flow and deform to allow peak stresses to be shared by neighboring elastic regions. This benefit becomes obvious when comparing the limited elastic strain OD with the available plastic strain DF. Analysis must assure that local flow does not lead to global yielding or fracture.

D. Triaxial Stress-Strain

The inelastic stress-strain relationship may be developed from Hooke's law,

$$\varepsilon_1 = \frac{1}{E_A} [\sigma_1 - \mu_n(\sigma_2 + \sigma_3)]$$

$$\varepsilon_2 = \frac{1}{E_A} [\sigma_2 - \mu_n(\sigma_1 + \sigma_3)] \tag{14}$$

$$\varepsilon_3 = \frac{1}{E_A} [\sigma_3 - \mu_n(\sigma_1 + \sigma_2)] \ ,$$

8

by replacing elastic constants with inelastic variables derived from uniaxial tests. E_A is the inelastic modulus, and Poisson's ratio, μ_n, is stress dependent; this ratio is different about each principal axis, thus constituting an orthotropic material. The most practical approach is to let the Poisson's ratio related to the largest stress represent the effective Poisson's ratio for all axes. Other options and consequences are discussed in section II-F. Assume σ_1 is the largest principal stress, and $\mu_n = \mu_1$. Squaring, adding equation (14), and collecting terms gives the combined stress-strain relationship over the entire inelastic range

$$[\varepsilon_1^2 + \varepsilon_2^2 + \varepsilon_3^2]\frac{E_A^2}{(1+2\mu_n)} = \sigma_1^2 + \sigma_2^2 + \sigma_3^2 - \left[\frac{4\mu_n - 2\mu_n^2}{1+2\mu_n^2}\right](\sigma_1\sigma_2 + \sigma_1\sigma_3 + \sigma_2\sigma_3) \ . \tag{15}$$

The right side of equation (15) is the combined principal stress expression, and is noted to be similar to the distortion energy expression, equation (13), which is related to the uniaxial tension stress,

$$\sigma_A = \left[\sigma_1^2 + \sigma_2^2 + \sigma_3^2 - \left[\frac{4\mu_n - 2\mu_n^2}{1+2\mu_n^2}\right](\sigma_1\sigma_2 + \sigma_1\sigma_3 + \sigma_2\sigma_3)\right]^{1/2} \ . \tag{16}$$

Letting $\sigma_2 = \sigma_3 = 0$, then $\varepsilon_2 = \varepsilon_3 = \mu_1\varepsilon_1$ and substituting into equation (15), provides the uniaxial relationships:

$$\frac{\sigma_A}{\varepsilon_A} = E_A \ , \tag{17}$$

$$\varepsilon_A = \left[\frac{\varepsilon_1^2 + \varepsilon_2^2 + \varepsilon_3^2}{(1+2\mu_n)}\right]^{1/2} \ . \tag{18}$$

Using equations (17) and (1), it follows that

$$\frac{1}{E_A} = \frac{\varepsilon_A}{\sigma_A} = \frac{\left[\frac{\sigma_A}{a}\right]^{1/b}}{\sigma_A}$$

or

$$\frac{1}{E_A} = \frac{[\sigma_A]^{(1-b)/b}}{[a]^{1/b}} \ . \tag{19}$$

Nondimensionalize equation (16) by dividing with σ_1^2, and substituting into equation (19), gives

$$\frac{1}{E_A} = \frac{\Phi}{\sigma_1}\left[\frac{\sigma_1}{a}\right]^{1/b} \ , \tag{20}$$

where

$$\Phi = \left[1 + \left[\frac{\sigma_2}{\sigma_1} \right]^2 + \left[\frac{\sigma_3}{\sigma_1} \right]^2 - \left[\frac{4\mu_n - 2\mu_n^2}{1 + 2\mu_n^2} \right] \left[\frac{\sigma_2}{\sigma_1} + \frac{\sigma_3}{\sigma_1} + \frac{\sigma_2\sigma_3}{\sigma_1^2} \right] \right]^{1-b/2b} \quad . \tag{21}$$

But equation (21) was developed in its simplest form by assuming Poisson's ratio independent of stress orientation, which is satisfied only at the elastic limit where $b = 1$ followed by $\Phi = 1$. Substituting equation (20) into equation (14) yields the desired combined stress-strain relationships:

$$\varepsilon_1 = \left(\frac{\sigma_1}{a} \right)^{1/b} \left[1 - \mu_1 \frac{\sigma_2}{\sigma_1} - \mu_1 \frac{\sigma_3}{\sigma_1} \right]$$

$$\varepsilon_2 = \left(\frac{\sigma_1}{a} \right)^{1/b} \left[\frac{\sigma_2}{\sigma_1} - \mu_1 \frac{\sigma_3}{\sigma_1} - \mu_1 \right] \tag{22}$$

$$\varepsilon_3 = \left(\frac{\sigma_1}{a} \right)^{1/b} \left[\frac{\sigma_3}{\sigma_1} - \mu_1 \frac{\sigma_2}{\sigma_1} - \mu_1 \right] \quad .$$

The associated stress relationships, solved from equation (22), are

$$\frac{\sigma_1}{\sigma_1} = \left(\frac{a}{\sigma_1} \right)^{1/b} \left[\frac{\varepsilon_1(1 - \mu_1) + \mu_1(\varepsilon_2 + \varepsilon_3)}{(1 - 2\mu_1)(1 + \mu_1)} \right]$$

$$\frac{\sigma_2}{\sigma_1} = \left(\frac{a}{\sigma_1} \right)^{1/b} \left[\frac{\varepsilon_2(1 - \mu_1) + \mu_1(\varepsilon_1 + \varepsilon_3)}{(1 - 2\mu_1)(1 + \mu_1)} \right] \tag{23}$$

$$\frac{\sigma_3}{\sigma_1} = \left(\frac{a}{\sigma_1} \right)^{1/b} \left[\frac{\varepsilon_3(1 - \mu_1) + \mu_1(\varepsilon_1 + \varepsilon_2)}{(1 - 2\mu_1)(1 + \mu_1)} \right] \quad .$$

E. Shear Properties

A shear stress-strain model is not only essential for analytical modeling, but for evaluating rosette strain gauges from structural test data. Published test data beyond the elastic limit is wanting. An approximation from uniaxial tension properties developed previously may be cautiously ventured. Recognizing that shear beyond the elastic limit is related to the same elastic-plastic slip phenomenon noted in figure 2, a two-parameter shear stress-strain expression is justified,

$$\tau = c \, \gamma^d \, , \tag{24}$$

and again the two parameters are determined from the extreme end conditions of the inelastic curve. The normal and shear stress-strain properties at the elastic limit end of figure 4 are established by

$$\frac{\sigma_{EL}}{\varepsilon_{EL}} = E \ , \quad \text{and} \quad \frac{\tau_{EL}}{\gamma_{EL}} = G = \frac{E}{2(1+\mu)} \ , \tag{25}$$

and related by the distortion energy equation (11) when all normal stresses are zero,

$$\tau = \frac{\sigma}{\sqrt{3}} \ . \tag{26}$$

Substituting equation (26) into the second part of equation (25) provides the elastic shear strain relation to the normal tension stress,

$$\gamma_{EL} = \frac{2}{\sqrt{3}} \frac{(1+\mu)}{E} \sigma_{EL} \ . \tag{27}$$

The ultimate shear strain may be derived from the assumption that the ultimate shear strain energy is equal to the ultimate normal strain energy,

$$\int_0^{\gamma_U} \gamma\tau d\gamma = \int_0^{\varepsilon_U} a\varepsilon^{(b+1)} d\varepsilon \ .$$

Substituting equation (26) for the shear stress and integrating gives the ultimate shear strain required to determine the shear parameter in equation (24),

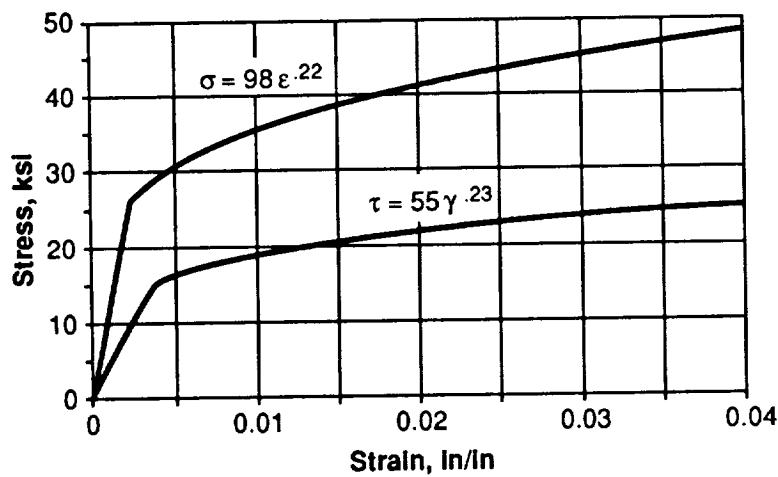$$\gamma_U \cong \varepsilon_U \sqrt{\frac{2\sqrt{3}}{b+2}} \ . \tag{28}$$

Figure 4. Derived shear stress-strain model.

11

The two parameters are calculated from

$$d = \frac{\log(\sigma_U/\sigma_{EL})}{\log(\gamma_U/\gamma_{EL})} \quad , \quad \text{and} \quad c = \frac{\sigma_{EL}}{\sqrt{3}\ \gamma_{EL}^d} \ . \tag{29}$$

F. Orthotropic Properties

Polycrystalline materials experience orthotropic properties when multiaxial stresses exceed the elastic limit. It was noted earlier in figure 1 that stressing beyond point A' and relaxing not only raised the elastic limit about one axis for the next cycle, but irrevocably used strain energy to cause permanent deformations about all axes. Properties about other axes remained the same as before uniaxial stressing, creating an orthotropic material.

If a triaxially stressed article is tested beyond the elastic limit and relaxed, the article is essentially "sprung," and boundaries are permanently changed. The article will not behave exactly as it did before, when the external load cycle is repeating through the elastic operational range, and should be a consideration in prototype testing. If the prototype is disassembled and reassembled according to specifications, the prototype will behave elastically in the operating range as before testing. Beyond the elastic range, the fixed orthotropic properties are subject to change only when exceeded.

In modeling inelastic substructures, boundaries are defined by the elastic global model. The substructure size selected must assure that remote inelastic stresses acting on the critical zone of interest do not spread to the elastic boundaries as the critical zone approaches the ultimate stress.

Poisson's ratio is a property affected by plastic flow which is directional, and irreversible, and it increases with stress. In a triaxial stress field, a different Poisson's ratio is expected for each stress axis. The only restriction imposed on Poisson's ratio is that the volume growth,

$$\frac{\Delta V}{V_o} = (1 + \varepsilon_x)(1 + \varepsilon_y)(1 + \varepsilon_z) - 1 \ , \tag{30}$$

at the elastic limit is established by the elastic Poisson's ratio, and that the volume growth at fully plastic flow is zero. Modifying equation (22) to assume orthotropic Poisson's ratio and substituting into equation (30) gives

$$\frac{\Delta V}{V_o} = \left[\frac{\sigma_x}{a}\right]^{1/b} \left[(1 - 2\mu_x)\frac{\sigma_x}{\sigma_x} + (1 - 2\mu_y)\frac{\sigma_y}{\sigma_x} + (1 - 2\mu_z)\frac{\sigma_z}{\sigma_x}\right], \tag{31}$$

after dropping high order terms.

At the elastic limit, all Poisson's ratios are equal to the elastic constant, and the volume growth becomes

$$\frac{\Delta V}{V_o} = \left[\frac{\sigma_x}{a}\right]^{1/b} (1 - 2\mu_e) \frac{(\sigma_x + \sigma_y + \sigma_z)}{\sigma_x} . \tag{32}$$

At the fully plastic extreme, equation (31) is satisfied only if

$$\mu_x = \mu_y = \mu_z = 0.5 . \tag{33}$$

But these extreme limitations in triaxial stress are identical to those discussed for uniaxial stress, which implies that Poisson's ratios are independent of each other and dependent only on stress or strain along their respective axes.

Since stress is the unknown variable in most structural problems, orthotropic Poisson's ratio related to multiaxial stress may sometimes complicate the solution. Generally, Poisson's ratio is not a very sensitive property, and a more practical approach is to assume the Poisson's ratio related to the greater stress is common to all axes. If triaxial stresses are close, then a common Poisson's ratio will provide very good results. If stress magnitudes span the total plastic range, then Poisson's ratios should be related to each respective strain where possible. Referring Poisson's ratio to the average of two strains is another option. Sensitivity analyses of Poisson's ratio as applied to critical models will identify the optimum option.

Sections V and VI are examples of orthotropic properties applied to biaxial stress problems. Note that Poisson's ratio in the denominator of equation (109) is related to dominant strain, ε_x, as suggested above. The maximum stress error that might develop from a maximum spread between ε_x and ε_z was estimated from the sensitivity equation (113). A 40-percent change in Poisson's ratio (75-percent change in strain) caused less than 4-percent error in stress conversion.

III. ANALYTICAL MODELING

The basic analytical technique is similar to the computational piece-wise linear method often used to solve nonlinear problems. Unique to this analytical development was relating all nonlinear material models to engineering stresses and strains in exponential form, and synthesizing them with existing strength of material stress and strain models. This simplified the algebra and allowed continuous integration for more descriptive results. The method uses existing principles of materials and strength familiar to most analysts, while circumventing plastic theory. It provides detailed insights to inelastic behavior. Models derived are related to the skirt structure and demonstrate the technique to be used for other models as required.

The specimen of figure 5 represents a bar or plate having a length L and a rectangular cross section of thickness t and width B normal to the page. External unit loads are the in-plane normal load, N, expressed in kips per inch, and the bending moment, M, expressed in kip-inches per inch. The bar specimen model, whose width and thickness are relatively equal, is amenable to one-dimensional stresses and is a convenient introduction to the mechanics of inelastic behavior.

13
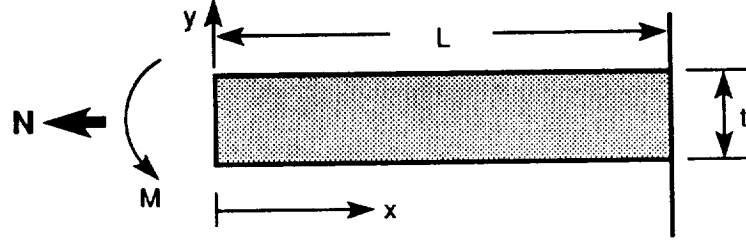
Figure 5. Specimen configuration and loading.

A. Normal Tension and Bending Models

Normal tension response models of rectangular bars is defined by uniaxial test parameters. The normal stress acting on the cross section of unit width is

$$\sigma_N = \frac{N}{t} , \tag{34}$$

and using equation (34), the corresponding strain is

$$\varepsilon_N = \left[\frac{N}{a\,t}\right]^{1/b} . \tag{35}$$

Pure bending moment M is constant along the length L and deforms into a cylindrical surface of radius r shown in figure 6. Since cross-sectional planes have been shown as remaining plane in elastic and plastic bending, the centroid $(t/2)$ of the rectangular cross section and the bending neutral axis are coincident from which the bending strain is linearly proportional to

$$\varepsilon_M = \frac{n}{m+n} = \frac{y}{r} . \tag{36}$$
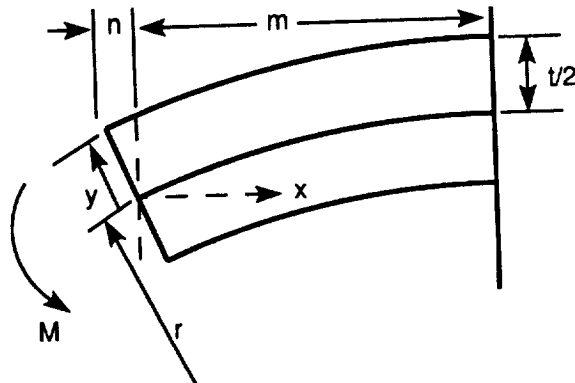
Figure 6. Pure bending geometry.

14

Substituting tensile strain from equation (36) into equation (1) gives the bending stress distribution,

$$\sigma_M = a\left[\frac{y}{r}\right]^b ,$$ (37)

along the cross section thickness as shown in figure 7.
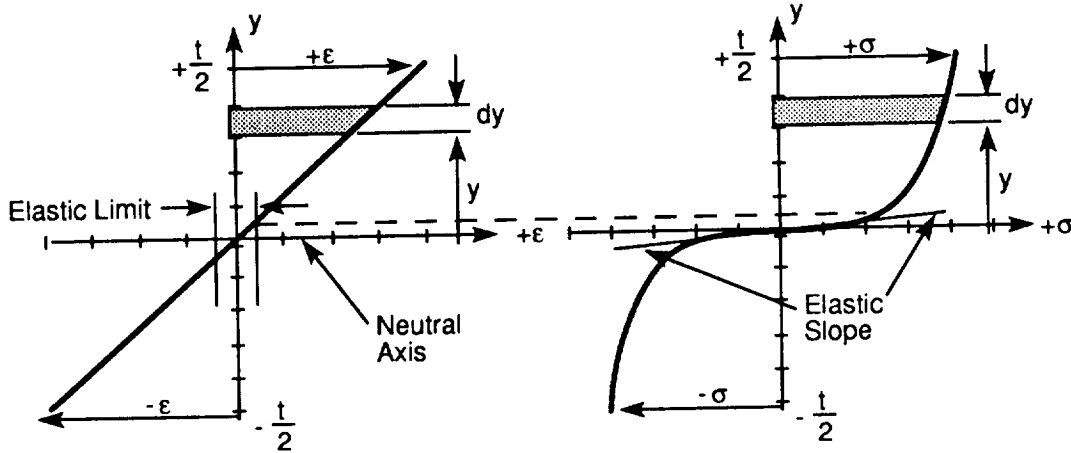
Figure 7. Bending stress and strain distribution.

The elemental area is $dA = B\,dy$ and the moment resulting from stresses acting on the sectional area is $dM = \sigma\,y\,dA$. Substituting the stress expression of equation (37) and integrating gives the total moment acting on the cross section,

$$M = a\int_{-t/2}^{t/2}\left[\frac{y}{r}\right]^b y\,dy = \frac{2a(t/2)^{b+2}}{(b+2)r^b} .$$ (38)

The specimen width B is taken as unity, and hereafter omitted in most derivations. Solving for the curvature from equation (38) and then equating with (37) gives

$$\frac{1}{r} = \left[\frac{(b+2)\,M}{2a(t/2)^{b+2}}\right]^{1/b} = \frac{2}{t}\left[\frac{\sigma_M}{a}\right]^{1/b} ,$$ (39)

from which bending stress at the extreme fibers is reduced to

$$\sigma_M = \pm\frac{2(b+2)\,M}{t^2} .$$ (40)

15

Note the elastic slope superimposed on the stress diagram, figure 7, is practically concurrent with the stress calculated from the nonlinear material model over the elastic range. This close fit is a measure of the accuracy expected from the analytical method. Also, note that when the strain hardening exponent, b, equals unity, the bending stress degenerates to the familiar elastic stress of a rectangular beam, as it should.

Bending strains at the extreme fibers were similarly derived by substituting the strain relationship of equation (36) into equation (39),

$$\varepsilon_M = \pm \left[\frac{2(b+2)\,M}{a\,t^2} \right]^{1/b} .$$

(41)

Bending transverse displacements may be derived from the moment and curvature relationship equation and from the slope expression, $\theta = dy/dx$. The slope is related to the curvature by

$$\frac{1}{r} = -\frac{d\theta}{dL} = -\frac{d^2y}{dx^2} .$$

(42)

Equating (39) with (42) gives

$$\frac{d^2y}{dx^2} = -\left[\frac{(b+2)\,M}{2a(t/2)^{b+2}} \right]^{1/b} ,$$

and multiplying both sides by dx and integrating yields the slope expression of the midplane at $x = 0$,

$$\theta = L \left[\frac{(b+2)\,M}{2a(t/2)^{(b+2)}} \right]^{1/b} .$$

(43)

Integrating again gives the transverse deflection at $x = 0$,

$$y = -\frac{L^2}{2} \left[\frac{(b+2)\,M}{2a(t/2)^{(b+2)}} \right]^{1/b} .$$

(44)

B. Combined Stresses

Shear-bending models have a wide variety of application and are essential for test analysis. Since no instrumentation is available to detect directly transverse shear V, a series of strain gauges measuring the variation of bending moment along the bar length L, figure 8, will provide the necessary data to determine the shear indirectly.

16
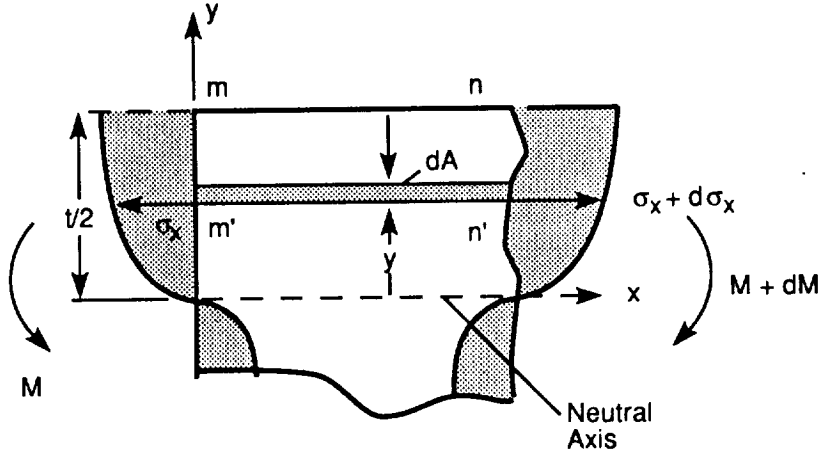
Figure 8. Combined bending-shear stress.

The moment, M, on the left interface is assumed to increase with distance, x, to $M + dM$ on the right interface. Induced stresses likewise increase from left to right. The stress-moment relationship is obtained by rearranging equation (37),

$$\frac{\sigma_M}{y^b} = \frac{a}{r^b} \ , \tag{45}$$

and substituting into equation (38) to solve for the moment induced stress,

$$\sigma_M = \frac{(b+2) \ y^b \ M}{2(t/2)^{b+2}} \ . \tag{46}$$

Since $\sigma_x = \sigma_M$, the force acting on the left interface is

$$\sigma_x \ dA = \frac{(b+2) \ y^b \ M}{2(t/2)^{b+2}} \ dA \ , \tag{47}$$

and

$$(\sigma_x + d\sigma_x) \ dA = \frac{(b+2) \ y^b}{2(t/2)^{b+2}} \ (M+dM) \ dA \ , \tag{48}$$

give the force on the right interface acting in the opposite direction. The net force is the difference of these two equations and is equal to the horizontal shear force in the $m' - n'$ plane,

$$\tau_{xy} \ B \ dx = \frac{dM(b+2)}{2(t/2)^{b+2}} \int_y^{t/2} y^b \ dA \ . \tag{49}$$

17

Substituting the beam shear force $V = dM/dx$, and the area $dA = B \, dy$ into equation (49) and then integrating gives the flexural shear stress expression,

$$\tau_{xy} = \frac{V(b+2)}{2(b+1)(t/2)^{b+2}} \left[(t/2)^{b+1} - y^{b+1} \right] .$$

(50)

The horizontal shear is equal to the vertical shear along the cross section thickness on the right interface. Since the maximum shear stress of equation (50) occurs at the neutral axis ($y = 0$), where the bending stress is minimum, the maximum combined stress must be calculated from the distortion energy theory of equation (11). Shear stresses vary along the cross section, but unlike pure bending, the associated strains cause plane sections to warp, and should be considered when combining with other applied loads.

Normal tension-bending stresses cannot be directly superimposed because they are not linearly related to strains, equation (34); nor is the bending neutral axis expected to coincide with the section centroid. However, an interacting model may be formulated by noting that normal strain ε_N is uniformly linear along the cross section, equation (35). Also, the bending strain is linearly proportional to the strain at the extreme fiber, ε_M, equation (36), because plane strains remain plane after pure bending. Since both axial strains are linear, they are algebraically added as shown in figure 9(A).

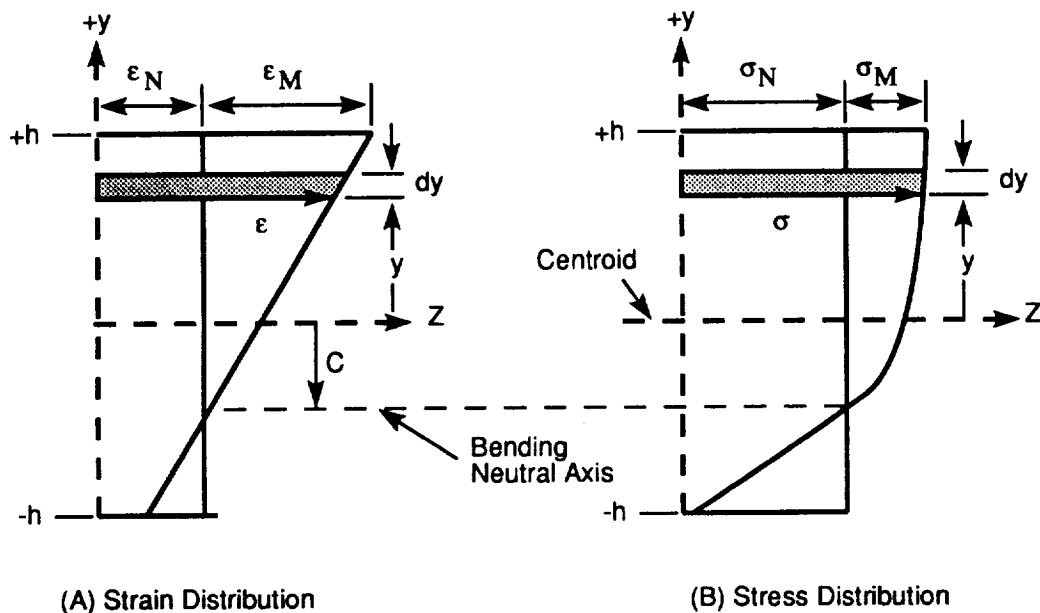(A) Strain Distribution   (B) Stress Distribution

Figure 9. Combined tension-bending distribution.

The net strain distribution is linear and proportional to the intersection of both strains at a point C below the cross sectional centroid. The net strain is defined by

$$\varepsilon = \varepsilon_N + \left[\frac{y - C}{h - C} \right] \varepsilon_M ,$$

(51)

where ε_M is the maximum bending strain at the extreme fiber having the same polarity as the normal load N. The neutral axis, C, is negative in the y-direction. The half-thickness, $t/2$, is replaced by h for simplicity of notation, and the normal strain of equation (35) is calculated from the given applied normal load, geometry, and material properties.

The combined stress distribution is shown on figure 9(B) and is determined by substituting equation (51) into equation (34) to give

$$\sigma = a \left| \varepsilon_N + \frac{(y-C)}{(h-C)} \, \varepsilon_M \right|^b \, \text{SGN}\left(\varepsilon_N + \frac{(y-C)}{(h-C)} \, \varepsilon_M \right) . \tag{52}$$

Expressions in absolute form allow raising strains to odd powers. SGN( ) is the signum function which reestablishes the sign of the expression. If its sign is positive, then the function equals $+1$ and the strain is positive. If the function equals -1, the strain is negative.

Solutions of the stress and strain distribution of equations (51) and (52) as a function of y rest with determining the unknown variables ε_M and C from the two static load equations; $dN(y) = \sigma(y) \, dy$, and $dM(y) = \sigma(y) \, y \, dy$. Substituting the stress expression of equation (52) into these static equations, the net normal load and total bending moment are

$$N = a \int_{-h}^{C} \left| \varepsilon_N + \frac{(y-C)}{(h-C)} \, \varepsilon_M \right|^b dy + a \int_{C}^{h} \left| \varepsilon_N + \frac{(y-C)}{(h-C)} \, \varepsilon_M \right|^b dy \tag{53}$$

and

$$M = a \int_{-h}^{C} \left| \varepsilon_N + \frac{(y-C)}{(h-C)} \, \varepsilon_M \right|^b y \, dy + a \int_{C}^{h} \left| \varepsilon_N + \frac{(y-C)}{(h-C)} \, \varepsilon_M \right|^b y \, dy \tag{54}$$

respectively. Integrating within the limits, the normal load and moment equations become

$$N = \frac{a(h-C)}{\varepsilon_M(b+1)} \, [\psi 1 - \psi 2] , \tag{55}$$

and

$$M = \frac{a(h-C)}{(b+1)\varepsilon_M} \left\{ \psi 2 \left[h + \frac{(h-C)}{(b+2)} \left[\frac{\varepsilon_N}{\varepsilon_M} - \frac{(h+C)}{(h-C)} \right] \right] + \psi 1 \left[h - \frac{(h-C)}{(b+2)} \left[\frac{\varepsilon_N}{\varepsilon_M} + 1 \right] \right] \right\} \tag{56}$$

where

$$\psi 1 = [ABS(\varepsilon_N + \varepsilon_M)]^{(b+1)} , \tag{57}$$

19

and

$$\psi 2 = \left[ABS\left(\varepsilon_N - \varepsilon_M \frac{(h+C)}{(h-C)}\right)\right]^{(b+1)} .$$

(58)

Given the geometric property h and combined loads N and M, the normal strain ε_N is calculated from equation (35). The bending strain at the extreme upper fiber ε_M and the bending neutral axis C are determined from equations (55) and (56), using the Newton-Raphson method presented in appendix A. Combined strain and stress distributions over the bar cross section may then be calculated by substituting the resulting bending strain and neutral axis values into equations (51) and (52), respectively. Conditions on figure 9 are that strains ε_N and ε_M have the same polarity, and that C is negative, but may be similarly modified for other conditions.

Results from this analytical normal tension-bending model are shown in figure 10. The linear bending strain distribution exhibited in the strain diagram, figure 10(B), is superimposed on the uniform normal strain, as in an elastic beam diagram. However, the neutral and centroid axes are not coincident, and the location of the distance C between them is defined by equilibrium conditions in the nonlinear stress diagram, figure 10(C). There the areas of bending tension and compression representing loads are equal and opposite which cancel the axial load. Their moments about the neutral axis add to balance the externally applied moment.
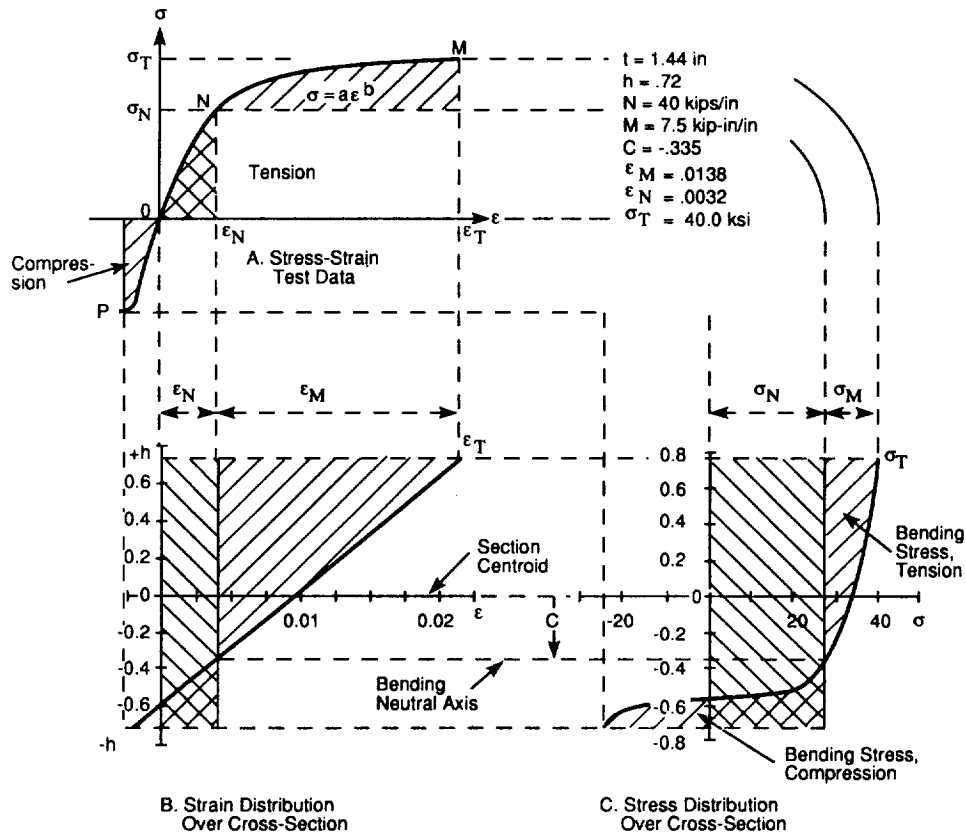

Figure 10. Combined normal tension-bending diagram.

The unsymmetrical shape of the stress profile may be understood by projecting select points from strain and stress diagrams onto the uniaxial stress-strain curve, figure 10(A). These projected points are labeled *PONM*. It is clear that large tension strain from bending loads projected on the shallow slope between points *N* and *M* produces relatively small stresses, which accounts for the projected narrow tension stress component into figure 10(C). On the other hand, small compression strains projected on the steep slope of *NOP* produce large stresses, which accounts for the very wide projected compression stress component.

Stress and strain responses demonstrated in the diagram have interesting implications on structural verification analysis. Back-to-back strain gauges are used to isolate pure normal strains from combined normal tension-bending strains. When testing in the elastic range, the pure normal strain is the average of two back-to-back strain gauge outputs. Beyond the elastic limit, this formula is not valid as revealed by the strain diagram. Though the bending stress is a third of the normal stress, the bending strain is over four times the normal strain. There is no direct method for isolating the normal strain from combined strain data except through an inelastic math model which is essential to support design, structural test, and operational analysis. The combined normal-bending loads model provides a firm basis for predicting failure. It is a prerequisite for sensitivity analyses leading to robust designs and operational load placards to increase safety margins for unique missions.

C. Plate Stresses and Strains

All of the previous bar models were derived for rectangular cross sections whose specimen width dimension B along the Z-axis is not much greater than the thickness t. These models form a special class of one-dimensional stress specimen. Another type structure is the two-dimensional stress specimen, such as plates and shells, having length and width dimensions many times greater than the thickness, and in which the stress normal to the plate is considered negligible. A plain stress condition is assumed to exist in plate problems.

Normal stress-strain relationships on plates may be derived by applying the plain stress conditions, $\sigma_y = 0$, to the second and third of equations (23) to obtain the associated strain,

$$\varepsilon_y = -\frac{\mu}{1-\mu} (\varepsilon_x + \varepsilon_z) . \tag{59}$$

Substituting equation (59) into the first and third of equations (23) gives the stress expressions in terms of biaxial strains,

$$\sigma_x = a\left[\frac{\varepsilon_x + \mu\varepsilon_z}{1-\mu^2}\right]^b ,$$

$$\sigma_z = \frac{a(\varepsilon_z + \mu\varepsilon_x)}{[1-\mu^2]^b} [\varepsilon_x + \mu\varepsilon_z]^{(b-1)} . \tag{60}$$

If the plate is subjected to uniaxial stress, in which $\sigma_z = \sigma_y = 0$, then the first part of equation (60) reverts to $\varepsilon_z/\varepsilon_y = -\mu$ which defines the uniaxial Poisson's ratio. The uniaxial strain is determined from the first of equations (22),

$$\varepsilon_x = \left[\frac{\sigma_x}{a}\right]^{1/b} ,$$

which, again, reverts to the uniaxial expression of equation (1). It may be concluded that a plate in uniaxial normal stress behaves as a bar specimen in which the stress is defined as

$$\sigma_x = \frac{N_x}{2h} , \tag{61}$$

where $h = t/2$.

Multiaxial property $(1 - \mu^2)$ was introduced into equation (60). Since the Poisson's ratio is related to the largest stress, it may be expressed as a two-parameter property for the compatibility reason given in section II,

$$\Gamma_x = (1 - \mu_x^2) = Q\sigma_x^R . \tag{62}$$

Poisson's ratio is calculated from equation (6) for end conditions μ_U at σ_U and μ_{EL} at σ_{EL}, and substituting into equation (62) gives

$$\Gamma_{xU} = [1 - \mu_{xU}^2] \quad \text{and} \quad \Gamma_{xEL} = [1 - \mu_{xEL}^2] . \tag{63}$$

Both parameters of equation (62) are calculated as in section II,

$$R = \frac{\log\left[\Gamma_{xU}/\Gamma_{xEL}\right]}{\log\left[\sigma_{xU}/\sigma_{xEL}\right]} \quad \text{and} \quad Q = \frac{\Gamma_{xEL}}{\sigma_{xEL}^R} . \tag{64}$$

Pure bending of plates results in a biaxial stress condition because the top surface is subjected to tension while the bottom is in compression simultaneously, and as in the bar specimen, produce lateral contraction and expansion from Poisson's ratio effects, figure 11. However, plate widths are very large compared to the thickness, forcing lateral strains at the top, bottom, and middle surfaces to be equally restrained to $\varepsilon_z = 0$ for continuity [7].

Invoking the plate condition and bending constraint, $\sigma_y = \varepsilon_z = 0$, into the third of equations (22),

22
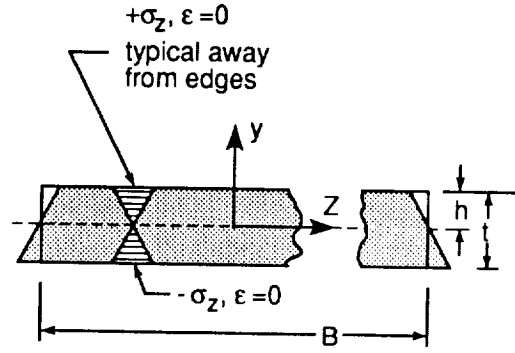
Figure 11. Poisson's ratio effect on plates in bending.

$$\varepsilon_z = 0 = \left[\frac{\sigma_x}{a}\right]^{1/b}\left[\frac{\sigma_z}{\sigma_x} - \mu_x\right],$$

the plate lateral strain is satisfied when

$$\frac{\sigma_z}{\sigma_x} = \mu_x \ . \tag{65}$$

Substituting equation (65) into the first and second of equations (22) gives the other two plate normal strains

$$\varepsilon_x = \left[\frac{\sigma_x}{a}\right]^{1/b} [1 - \mu_x^2] \ ,$$

$$\tag{66}$$

$$\varepsilon_y = \left[\frac{\sigma_x}{a}\right]^{1/b} [- \mu_x - \mu_x^2] \ .$$

Substituting equation (62) into the first of equations (66), the axial strain is rewritten as

$$\varepsilon_x = Q \ \sigma_x^R \left[\frac{\sigma_x}{a}\right]^{1/b} = Q\left[\frac{\sigma_x^{b/\beta}}{a}\right]^{1/b} , \tag{67}$$

where the combined exponent is defined by

$$\beta = \frac{b}{1 + bR} \ . \tag{68}$$

23

Equating (36) with (67) gives the axial stress through the thickness

$$\sigma_x = \left[\frac{y}{r}\right]^\beta \left[\frac{a}{Q^b}\right]^{\beta/b} . \tag{69}$$

This stress acting over the plate cross section produces a moment, $dM = \sigma_x \, y \, dy$. Integrating over the thickness, solving for the curvature,

$$\frac{1}{r} = \left[M\left[\frac{\beta+2}{2h^{(\beta+2)}}\right]\left[\frac{Q^b}{a}\right]^{\beta/b}\right]^{1/\beta} , \tag{70}$$

and substituting equation (70) into equation (69) yields the plate bending stresses at the extreme fibers

$$\sigma_M = \pm M\left[\frac{\beta+2}{2h^2}\right] . \tag{71}$$

Substituting equation (70) into (36) gives the bending strain over the thickness,

$$\varepsilon_x = \left[y^\beta M\left[\frac{\beta+2}{2h^{(\beta+2)}}\right]\left[\frac{Q^b}{a}\right]^{\beta/b}\right]^{1/\beta} , \tag{72}$$

and at the extreme fibers,

$$\varepsilon_M = \pm\left[M\left[\frac{\beta+2}{2h^2}\right]\left[\frac{Q^b}{a}\right]^{\beta/b}\right]^{1/\beta} . \tag{73}$$

The slope expression at $x = 0$ is derived by equating (70) with (42) and integrating,

$$\theta = L\left[M\left[\frac{\beta+2}{2h^{(\beta+2)}}\right]\left[\frac{Q^b}{a}\right]^{\beta/b}\right]^{1/\beta} . \tag{74}$$

Integrating again over the length, gives the deflection at $x = 0$,

$$y = -\frac{L^2}{2}\left[M\left[\frac{\beta+2}{2h^{(\beta+2)}}\right]\left[\frac{Q^b}{a}\right]^{\beta/b}\right]^{1/\beta} . \tag{75}$$

The bending shear stress expression is analogous to the bar stress, using plate combined exponent, β,

24

$$\tau_{xy} = \frac{V\ (\beta+2)[h^{(\beta+1)} - y^{(\beta+1)}]}{2(\beta+1)\ h^{(\beta+2)}} \quad . \tag{76}$$

Combined bending and normal loads interaction equations were derived similarly to the bar specimen above. Substituting equation (61) into (1) gives the normal strain as a function of the known applied axial load,

$$\varepsilon_N = \left[\frac{N}{2ah}\right]^{1/b} \quad . \tag{77}$$

The combined normal and bending strains acting over the cross section are expressed by equation (51). The bending stress over the section is obtained from equations (36) and (69),

$$\sigma_M = \left[\frac{a^{(1/b)}}{Q}\right]^{\beta} ABS\left|\varepsilon_M \frac{(y-c)}{(h-c)}\right|^{\beta} SGN\ (y-c) \quad . \tag{78}$$

The normal uniaxial stress is defined by equation (1),

$$\sigma_N = a\varepsilon_N^{\ b} \quad ,$$

which may be modified to conform with equation (78) by multiplying and dividing material parameters,

$$\sigma_N = \left[\varepsilon_N^{\ b/\beta}\ Q\ a^{(b-\beta)/b\beta}\right]^{\beta}\left[\frac{a^{(1/b)}}{Q}\right]^{\beta} \quad .$$

But

$$\varepsilon_N^{\ b/\beta}\ Q\ a^{(b-\beta)/b\beta} \cong \varepsilon_N \quad ,$$

so that the combined stress equation is simplified as

$$\sigma_T = \left[\frac{a^{(1/b)}}{Q}\right]^{\beta} ABS\left|\varepsilon_N + \varepsilon_M \frac{(y-c)}{(h-c)}\right|^{\beta} SGN\left(\varepsilon_N + \varepsilon_M \frac{(y-c)}{(h-c)}\right) \quad . \tag{79}$$

The net force acting on the cross section is $dN(y) = \sigma_T(y)\ dy$, and integrating over the limits $-h$ to C, and C to $+h$ gives

25

$$N = \frac{(h-C)\,[\psi 3 - \psi 4]}{(\beta+1)\,\varepsilon_M}\left[\frac{a^{1/b}}{Q}\right]^{\beta} , \tag{80}$$

$$M = \frac{(h-C)}{(\beta+1)\,\varepsilon_M}\left[\frac{a^{1/b}}{Q}\right]^{\beta}\left\{\psi 4\left[h+\frac{(h-C)}{(\beta+2)}\left[\frac{\varepsilon_N}{\varepsilon_M}-\frac{(h+C)}{(h-C)}\right]\right]+\psi 3\left[h-\frac{(h-C)}{(\beta+2)}\left[\frac{\varepsilon_N}{\varepsilon_M}+1\right]\right]\right\} , \tag{81}$$

where

$$\psi 3 = [ABS\,(\varepsilon_N+\varepsilon_M)]^{(\beta+1)} , \tag{82}$$

and

$$\psi 4 = \left[ABS\left(\varepsilon_N-\varepsilon_M\frac{(h+C)}{(h-C)}\right)\right]^{(\beta+1)} . \tag{83}$$

Given the geometry, material, and applied axial normal and bending loads, the bending neutral axis C and bending strain ε_M are solved simultaneously from equations (80) and (81) through Newton-Raphson method presented in appendix A. The stress and strain profiles over the plate thickness are calculated from equations (51) and (79).

IV. FEM VERSUS ANALYTICAL MODELS

Two independent global and substructural models of the SRB aft skirt were developed using the ANSYS and NASTRAN commercial codes. Both substructural predictions of the critical weld region were in good agreement with gauge measurements on the structural test article throughout the elastic range. Beyond the elastic limit, the weld failed very short of predictions. Given that analytical methods solve few simple problems accurately and that FEM solves many complex problems approximately, the focus of the following analysis was to assess the nature and reasonableness of FEM approximations.

The ANSYS finite element method was selected [6] because of its built-in graphic and contour mapping capability. The material behavior option used was the multilinear kinematic hardening (KH), and the element was a three-dimensional utilization brick (eight-node isoparametric) that was applied in the aft skirt structural model. Because a brick element is often used to fine tune predictions of triaxial stress zones having the highest potential for failure, it was the most critical and logical element to be explored.

A common materials model was defined to be compatible with the ANSYS and analytical methods using equations (2) and (3),

$$\sigma = 87\,\varepsilon^{0.2} , \tag{84}$$

based on assumed uniaxial properties $\sigma_{FL} = 26.3$ ksi, $\sigma_U = 45.7$ ksi, $\varepsilon_U = 0.04$, and $E = 10,500$ ksi. The ANSYS code defines Poisson's ratio similar to equation (6),

$$\mu = 0.5 - 0.2\left[\frac{E_S}{E}\right],$$

where E_S is the secant modulus. The analytical method used the same formula which reduced to

$$\mu = 0.5 - 95,000 \; \bar{\sigma}^{4.0} . \tag{85}$$

All other properties required for this method comparison are defined above and may be generated by the plate specimen program in appendix A.

Two simple structures, as in figure 5, were modeled, both specimens having a length of 6 in and a thickness of $t = 1.44$ in. The bar specimen had a width B of 1 in. The plate specimen had a width of 7 in to exercise the continuity condition in bending. Pure bending and tension loads were applied independently and combined on both specimens providing sufficient number and variety of cases for comparison and cross checking. Loads were selected to produce stresses on the outermost fiber in excess of the elastic limit.

A. Bar Specimen

Results from the analytical method were based on equations (34), (35), (40), (41), (51), and (52) combined with the stress program in appendix A. Results from the FEM were based on data taken at the specimen midwidth and uppermost brick to represent typical stresses away from edge conditions. A comparison of the two sets of results, table 1, shows that Poisson's ratios compared well, but analytical bending strains ranged up to 20 percent higher than ANSYS.

Table 1. Analytical versus ANSYS results of bar specimen.

A	B	C	D	E	F	G	H
N	M	Analytical Method			ANSYS Code		
kip/in	kip-in per in	Stress ksi	Strain in/in	μ	Stress ksi	Strain in/in	μ
40	0	27.7	.0033	.34	27.2	.0032	.34
50	0	34.7	.0101	.43	35.1	.0100	.44
60	0	41.7	.0252	.47	42.4	.0228	.48
0	15	31.8	.0065	.41	31.7	.0062	.39
0	18	38.2	.0163	.45	37.1	.0139	.44
0	20	42.4	.0276	.47	41.0	.0225	.45
40	2.5	33.2	.0080	.42	31.8	.0066	.41
40	7.5	39.7	.0197	.46	39.1	.0182	.47
40	10	43.3	.0304	.47	42.6	.0275	.48

Recalling that FEM data output relates to the average value of the outermost element, FEM bending strain predictions are expected to fall short of surface prediction (fig. 12). This error increases with increasing moment and with decreasing number of bricks modeling the thickness. It is a characteristic error that applies to elastic bending stresses and strains as well as plastic strain computations. By extending the ANSYS linear strain plot to the surface, the modified strains came to within 5-percent agreement. This match on all three loading models, and notably on the intricate combined loading model, established a mutual credibility of the analytical and FEM approaches with a one-dimensional stress specimen.
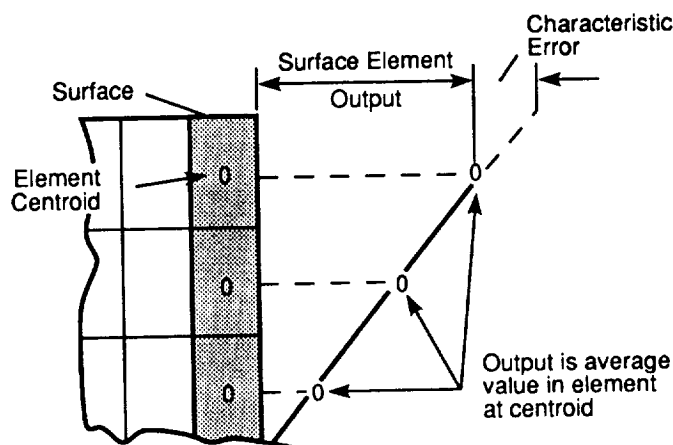
Figure 12. FEM characterisitic surface error.

B. Plate Specimen

The ANSYS computational method was applied to the 7-in width specimen with no other change from the previous bar specimen computation. The analytical approach was similar to that of the bar specimen, except that plate equations (77) through (81), combined with the plate program in appendix A, were imposed on the specimen. Results are presented in table 2.

Table 2. Analytical versus ANSYS results of plate specimen.

A	B	C	D	E	F	G	H
N	M	Analytical Method			ANSYS Code		
kip/in	kip-in per in	Stress ksi	Strain in/in	$-\frac{\varepsilon_Z}{\varepsilon_X}$	Stress ksi	Strain in/in	$-\frac{\varepsilon_Z}{\varepsilon_X}$
40	0	27.7	.0033	.34	27.6	.0031	.32
50	0	34.7	.0101	.43	36.4	.0089	.35
60	0	41.7	.0252	.47	45.0	.0204	.29
0	15	31.8	.0059	0	32.2	.0056	.37
0	18	38.2	.0141	0	37.7	.0105	.41
0	20	42.4	.0231	0	41.9	.0154	.42
40	2.5	33.2	.0069	.34	32.5	.0057	.34
40	7.5	39.7	.0162	.34	40.7	.0137	.35
40	10	43.3	.0245	.34	44.3	.0193	.34

In comparing the plate specimen results, the FEM responses in columns F, G, and H due to axial normal loads only ($M = 0$) should be identical to those in table 1, since both specimens act in uniaxial tension, as discussed in section III-C. Contrarily, plate model strains in column G are shown lower than column D, and table 1, implying a lateral constraint, $\varepsilon_z = 0$, where none was intended. If such a lateral constraint was imposed, strain ratios in column H would be naught, but in fact, FEM strain ratios are large. The ANSYS results of the uniaxially stressed plate as modeled are bewildered.

The most naked departure between the analytical and FEM plate results was noted in the pure bending model for $N = 0$ and $M = 15$ through 20. It is generally established [7] that elastic plates in bending must assume zero lateral strain, $\varepsilon_z = 0$, at both surfaces and midplane away from edges in order to satisfy the continuity condition illustrated in figure 11. The FEM lateral strains derived from column H are about a third of the axial strains, which clearly fails to comply with plate lateral constraint. This ANSYS fault is further manifested by the very small axial strain prediction in column G. Strains in column D represent the lower limits.

The same surface characteristic error of figure 12 was observed in the FEM plate bending model which resulted in submarginal predictions. The standard remedy is to increase the brick elements across the thickness until the strains in surface elements converge. Since doubling the brick numbers more than doubles the machine time, subdividing only the surface elements within the aspect ratio limit should be a more prudent course.

The net effects of plate continuity condition and FEM surface error may cause strain predictions to be 50 percent less than expected when compared with the analytical method. The ANSYS contour mapping feature does locate peak stress areas very well. Most patterns and trends may be valid, but intensities should be checked by other methods.

Based on deficiencies demonstrated by the results of two different loading conditions, it seems that the ANSYS brick element as presently modeled with the plastic option may be inadequate to predict plate strains and associated stresses in critical two- and three-dimensional stress regions.

The analytical method served to expose a conflict with the FEM plastic plate option, but the ANSYS elastic option with piece-wise nonlinear material input might have served as well. In fact, the ANSYS elastic piece-wise approach is recommended for primary inelastic computations (or backup) until the plastic option deficiency is resolved. Element number and sizes must be checked on all FEM for convergence of bending strains within reasonable tolerances.

V. BUTT-WELD STRESSES

Butt-welds are preferred joints for permanent assemblies because their mechanical behavior is uniform and undistinguishable from the connected base plate under normal operating loads. Beyond the elastic limit, dissimilar joint material properties and geometries promote stresses which influence the ultimate safety factor. The material discontinuity stress discovery was reported [1] in an exploration mode and is here synthesized into the ensuing analytical method.

Figure 13 is a square groove configuration of butt-welded plates. The plates are milled base material. The weld filler is usually the same base material with added substances to improve wetted surfaces and flow properties. The governing weld geometry is simply the thickness *t* limited by adjoining plate geometry requirements, and width *w* is usually decided by manufacturing considerations discussed before.
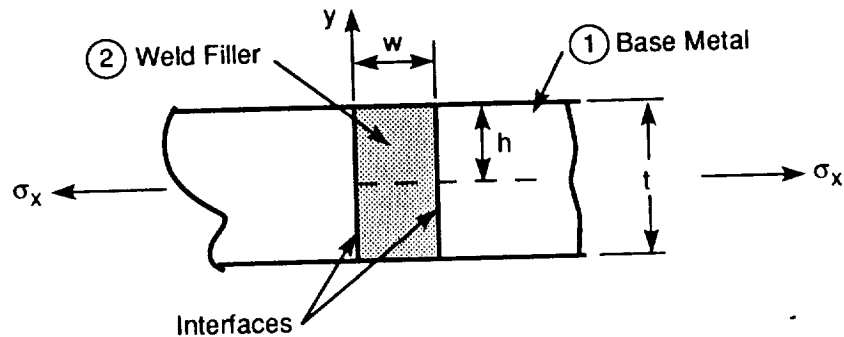

Figure 13. Butt-weld specimen.

A. Material Discontinuity

Structural areas with greatest potential for yield and failure are often identified by severe, local discontinuities of loads, temperature, geometry, dissimilar base materials, and combinations. Another type of discontinuity is the insidious butt-weld of the same base materials; but interfacing materials exhibit sufficiently different mechanical properties beyond the elastic limit to cause local distortion. Property differences are primarily a result of the manufacturing process, such as HAZ gradient, casting semblance of filler, filler metal additives, work hardening, and heat treatment variations. In any case, the phenomenon and analysis at their interface are the same.

When two such materials in tandem are subjected to a common axial stress, σ_x, they exhibit a common strain and Poisson's ratio up to the elastic limit. Beyond the elastic limit, properties of materials 1 and 2 bifurcate to establish their independent stress-strain and stress-Poisson's ratio relationships, which produces two different axial strains (ε_1 and ε_2) and two Poisson's ratios (μ_1 and μ_2) as illustrated in figure 14. Because this difference of properties is the source of interface discontinuities, their relationship to stress must be redefined with their new origin at the bifurcation.
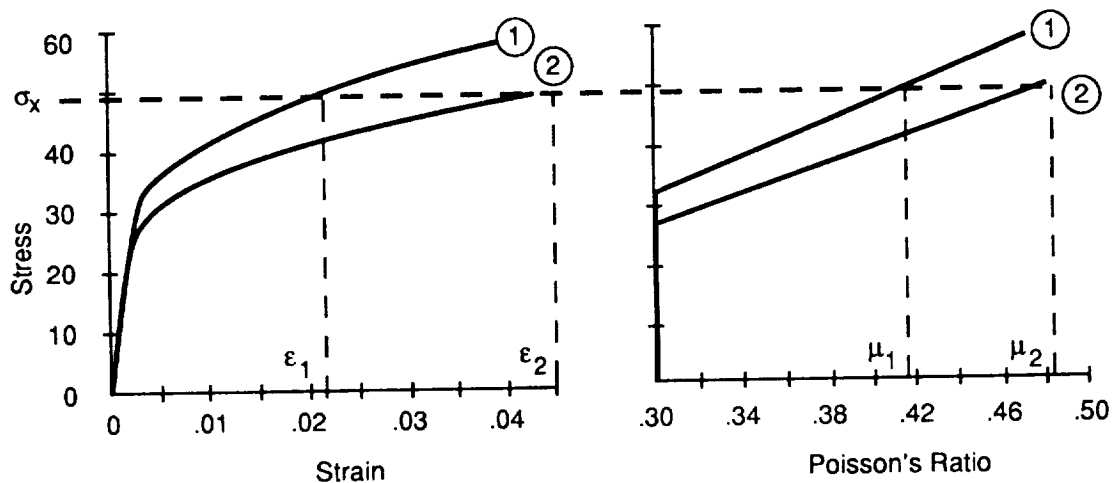

Figure 14. Properties of two materials under common stress.

The uniaxial stress-strain expression should be similar to the two-parameter form of equation (1),

$$(\sigma_x - \sigma_{EL,2}) = A[\varepsilon_x - \varepsilon_{EL,2}]^B , \tag{86}$$

where subscript *EL,2* refers to the new origin, which is the elastic limit of weakest element, 2. Given ultimate and elastic limit stresses and strains of each element, and using equation (1) to calculate immediate stresses, $\sigma_{k,1}$ and $\sigma_{k,2}$, at a suitable strain of weakest element,

$$\varepsilon_{k,2} = \frac{\varepsilon_{U,2}}{3} , \tag{87}$$

the exponent and coefficient of each element is computed as before,

$$B = \frac{\log[(\sigma_U - \sigma_{EL,2})/(\sigma_k - \sigma_{EL,2})]}{\log[(\varepsilon_U - \varepsilon_{EL,2})/ (\varepsilon_{k,2} - \varepsilon_{EL,2})]} , \tag{88}$$

$$A = \frac{\sigma_k - \sigma_{EL,2}}{[\varepsilon_{k,2} - \varepsilon_{EL,2}]^B} . \tag{89}$$

The two-parameter stress Poisson's ratio relationship is similarly developed. Using equations (5) through (9) and (1), Poisson's ratios,

$$\mu = g\left[\frac{\sigma}{a}\right]^{f/b} , \tag{90}$$

are calculated at ultimate stress for each element, $\mu_{U,1}$ and $\mu_{U,2}$. Intermediate stresses, $\sigma_{\mu k,1}$ and $\sigma_{\mu k,2}$, are calculated for $\mu_k = 0.36$ from equation (90),

$$\sigma_{\mu k} = a\left[\frac{\mu_k}{g}\right]^{b/f} . \tag{91}$$

The stress-Poisson's ratio property beyond the elastic limit is

$$(\mu_x - \mu_{EL}) = G[\sigma_x - \sigma_{EL}]^F , \tag{92}$$

and the two parameters are determined from

31

$$F = \frac{\log[(\mu_U - \mu_{EL.2})/(\mu_k - \mu_{EL.2})]}{\log[(\sigma_U - \sigma_{EL.2})/(\sigma_k - \sigma_{EL.2})]} \quad , \tag{93}$$

and

$$G = \frac{(\mu_k - \mu_{EL.2})}{[\sigma_{\mu_k} - \sigma_{EL.2}]^F} \quad . \tag{94}$$

The specimen of figure 13 is in a plane stress condition defined by $\sigma_z = 0$. Substituting this condition into the second of equations (22), the uniform lateral strain on either element subjected to axial stress, σ_x, is

$$\varepsilon_y = -\mu_x \left[\frac{\sigma_x}{a}\right]^{1/b} \quad ,$$

and after exceeding the elastic limit, the lateral strain assumes properties of equations (86) and (92),

$$(\varepsilon_y - \varepsilon_{EL.2}) = -G[\sigma_x - \sigma_{EL.2}]^F \left[\frac{\sigma_x - \sigma_{EL.2}}{A}\right]^{1/B} \quad ,$$

which reduces to

$$(\varepsilon_y - \varepsilon_{EL.2}) = -\frac{G}{A^{(1/B)}} [\sigma_x - \sigma_{EL.2}]^{(FB+1)/B} \quad . \tag{95}$$

Lateral contraction on each element resulting from the lateral strain of equation (95) is calculated from

$$v = \int_0^h (\varepsilon_y - \varepsilon_{EL.2}) \, dy \quad . \tag{96}$$

Applying equation (96) to the two elements of different materials subjected to a common axial stress, a lateral mismatch occurs at the free interface as shown in figure 15(A) and expressed by

$$v_1 - v_2 = -\frac{h \, G1}{A1^{(1/B1)}} [\sigma_x - \sigma_{EL.2}]^{(F1 \times B1 + 1)/B1} + \frac{h \, G2}{A2^{(1/B2)}} [\sigma_x - \sigma_{EL.2}]^{(F2 \times B2 + 1)/B2} \quad .$$

32

Dividing by the last term, and neglecting the stress with the exponent having small differences between material properties of the same metallic base, the net lateral displacement of the two different materials elements at the free interface reduces to

$$v_\sigma = v_1 - v_2 = h \frac{G2}{A2^{(1/B2)}} [\sigma_x - \sigma_{EL,2}]^{(F2 \times B2 + 1)/B2} \left[1 - \frac{G1\ A2^{(1/B2)}}{G2\ A1^{(1/B1)}}\right].$$ (97)

But elements 1 and 2 were bonded at the interface in an unloaded condition. In applying the axial load, the constrained interface caused local distortion as shown in figure 15(B). This distortion is the symptom of discontinuity stresses. A math model was devised in appendix B which consisted of an externally applied unit load q abruptly ending at a distance d, representing the interface of one material element. The abrupt load change simulated normal and shear discontinuity stresses at the boundary, which propagated through the weld (weakest) element. These discontinuity stress distributions were derived from classical mechanics, and results are stated in equation (B-9) in nondimensional form.

The unit loading q of figure B-1 acts normal (y-axis) to the element, and because of the orthotropic nature of polycrystalline materials, lateral material properties are independent of equations (86) and (92). Applying plane stress conditions to the second of equations (22), the lateral strain is

$$\varepsilon_y = \left[\frac{q}{a}\right]^{1/b} \left[\frac{\sigma_y}{q} - \mu_x \frac{\sigma_x}{q}\right].$$ (98)

Substituting these parameters, and the first and second of equations (B-9) into (98) gives the displacement

$$\overline{v} = \left[\frac{q}{a}\right]^{1/b} \int_0^h [Dy - \mu Dx]\ dy\ .$$ (99)

In reviewing the stress distributions along the half-thickness in figure B-3, the D_x component is noted to describe equal positive and negative areas, which implies that the intergration over the thickness would negate its contribution to lateral displacement in equation (99). Deleting D_x and integrating gives the lateral displacement at the boundary as a function of the dummy loading,

$$\overline{v} = \frac{h}{Ks} \left[\frac{q}{a}\right]^{1/b}\ ,$$ (100)

where

$$\frac{1}{Ks} = T + 4 \sum_1^m \sin \alpha T \cos \alpha T \left[\frac{e^{-\alpha H}}{\alpha H}\right] \left[H \cosh \alpha H - \left(H + \frac{2}{\alpha}\right)\sinh \alpha H\right].$$ (101)
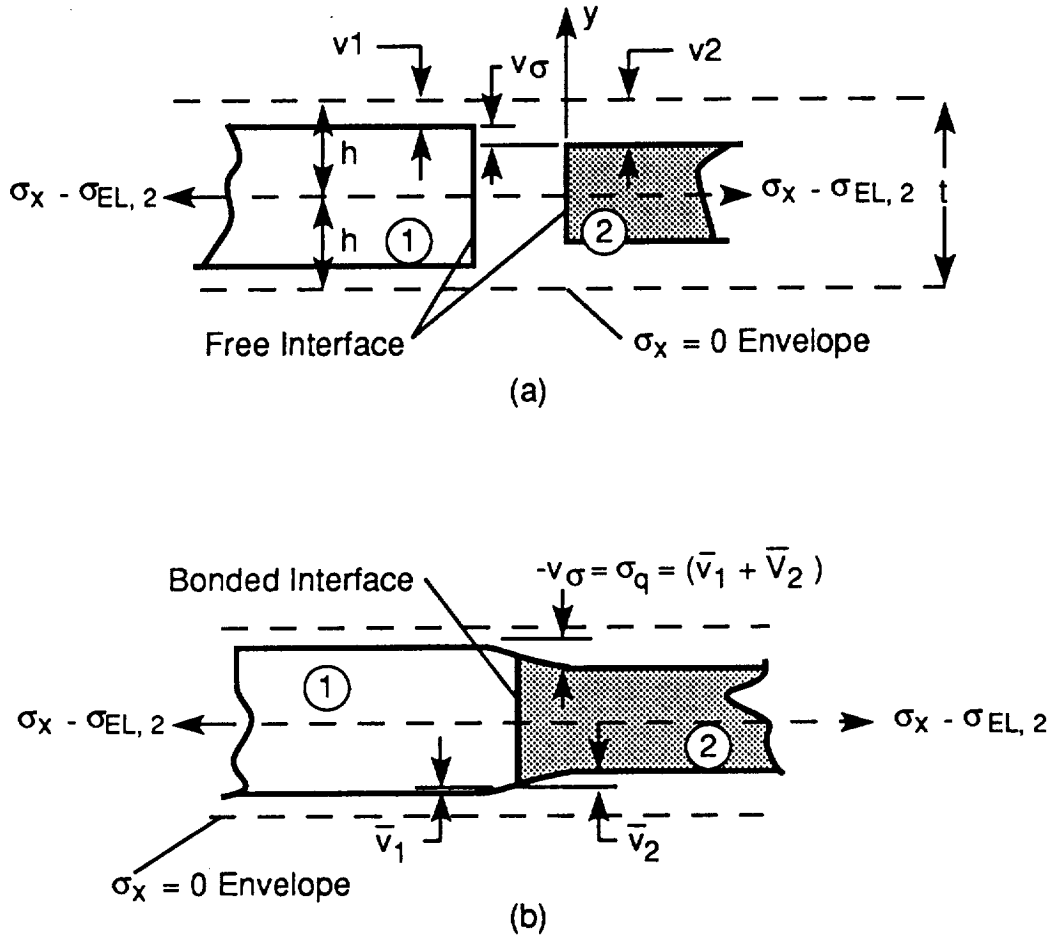
Figure 15. Material discontinuity displacements.

To match the net displacement of figure 15(b), the external dummy unit load in equation (100) must compress element 1, and stretch element 2 with equal and opposite intensity,

$$\overline{v}_q = \overline{v}_1 + \overline{v}_2 = \left[1 + \frac{a_2^{(1/b_2)}}{a_1^{(1/a_1)}} \right] \frac{h}{Ks} \left[\frac{q}{a_2} \right]^{1/b_2} . \tag{102}$$

Substituting equations (97) and (102) into the bonded interface equilibrium condition, $v_\sigma + v_q = 0$, the external dummy-to-axial unit loads ratio is

34

$$\frac{q}{[\sigma_x - \sigma_{EL,2}]^{\zeta}} = Kq \ , \tag{103}$$

where

$$Kq = a_2 \left[\frac{G2\ Ks}{A2^{1/B2}} \left[1 - \frac{G1\ A2^{1/B2}}{G2\ A1^{1/B1}} \right] \frac{a_1^{1/b_1}}{a_1^{1/b_1} + a_2^{1/b_2}} \right]^{b_2} , \tag{104}$$

and

$$\zeta = \frac{b_2\ (F2 \times B2 + 1)}{B2} . \tag{105}$$

Finally, multiplying equations (103) and (B-9) eliminates the dummy load q and produces the desired discontinuity stress distributions at the interface as a function of applied axial stress beyond the elastic limit,

$$S_x = \left[\frac{\sigma_{0x}}{q} \right] \frac{q}{[\sigma_x - \sigma_{EL,2}]^{\zeta}} = D_x\ Kq \ ,$$

or,

$$S_x = \frac{\sigma_{0x}}{[\sigma_x - \sigma_{EL,2}]^{\zeta}} = D_x\ Kq$$

$$S_y = \frac{\sigma_{0y}}{[\sigma_x - \sigma_{EL,2}]^{\zeta}} = D_y\ Kq \tag{106}$$

$$S_{xy} = \frac{\sigma_{0xy}}{[\sigma_x - \sigma_{EL,2}]^{\zeta}} = D_{xy}\ Kq \ ,$$

where $\sigma_x > \sigma_{EL,2}$ and $\sigma_{EL,2}$ refer to the weakest element, 2. Most relevant to a designer is the maximum stress factor occurring at the applied ultimate stress of the weakest material. Equations (107) are the ratios of stress components with the ultimate stress:

$$S_{Ux} = \frac{D_x\ Kq}{\sigma_{U,2}} [\sigma_{U,2} - \sigma_{EL,2}]^{\zeta}$$

$$S_{Uy} = \frac{D_y\ Kq}{\sigma_{U,2}} [\sigma_{U,2} - \sigma_{EL,2}]^{\zeta} \tag{107}$$

$$S_{Uxy} = \frac{D_{xy}\ Kq}{\sigma_{U,2}} [\sigma_{U,2} - \sigma_{EL,2}]^{\zeta} .$$

Figure 16 presents the discontinuity stress factors distribution along the interface from mid-thickness to surface, as defined by equation (107), using properties from figure 14. The weld geometry assumed was that of the SRB skirt, $t/w = 5.75$. Note that the shear stress component is largest and occurs at $y/h = 0.96$. It is not possible to experimentally measure this shear because it is transverse, and because it occurs just below the surface. The shear distribution is very sharp, and it required 42 points to focus the peak and would have eluded most FEM modelers using six element thickness selection. The peak value was compromised further because an element averages the stresses over each brick thickness. Nevertheless, shear presence was hypothesized by Mr. Paul Munafo from a metallurgical viewpoint during the skirt failure review, but it could not be supported by mechanics at that time. Because material models are so arduous, a program to calculate them and stresses of equation (107) is presented in appendix B.

The failure expression of equation (11) may be used to compute the combined discontinuity stress factor at the interface. Including a factor of one onto the x-stress component to account for the externally applied axial stress, the combined stress factor is

$$S_{Uc} = \sqrt{(1 + S_{Ux})^2 + S_{Uy}^2 - (1 + S_{Ux})\ S_{Uy} + 3S_{Uxy}^2}\ . \tag{108}$$

The material discontinuity stress factor for the above butt-weld example was 1.11, which occurred 1/32-in below the weld surface.
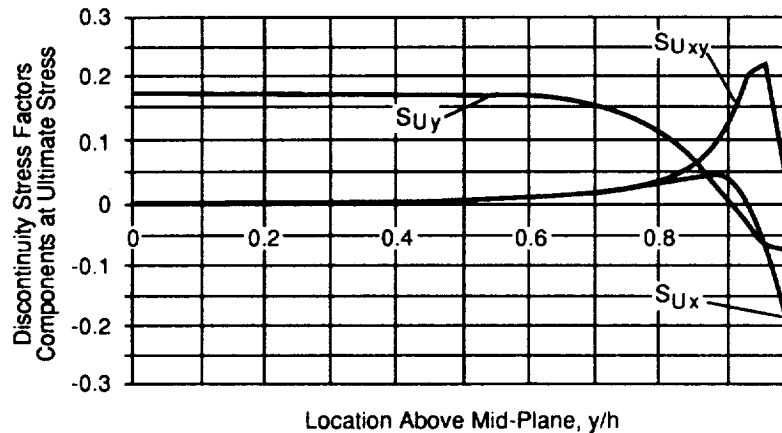
Figure 16. Discontinuity stress factors along weld interface.

B. Geometric Effects

Benefits of improved specific strength materials in high performance shell structures are often tempered by joint weaknesses and further discounted by joint geometric limitations. Butt-weld simple geometric parameters were examined for inelastic mechanics effects using models developed in sections II and III.

Applied Inplane Stresses: Discontinuity stresses were calculated for plate specimen of butt-welds having a thickness-to-width ratio of $t/w = 5.75$, figure 16. Other ratios were varied over a practical range to ascertain the existence of a weld geometry that would decrease the peak stress factors at the interface.

The governing parameter was a stress factor Kq of equation (104). Using the same material properties and location of maximum combined stress, $y/h = 0.96$ observed in figure 16, a combined discontinuity stress factor of 1.11 was noted to occur over a range of $t/w = 1$ to 7. Based on these results, there is no requirement from the mechanics viewpoint to control it. The overwhelming geometric consideration seems to be the heat sink effects and associated thermal distortions induced into the structure.

Test specimens of weld joints are usually shaped with nearly square test cross sections which impose triaxial stress conditions and with unique material discontinuity stress factors at the weld interface. However, most butt-weld joint applications are on plates having cross sections of very large aspect ratios which result in a two-dimensional stress field causing the discontinuity stresses defined above. From the designer's viewpoint, it is necessary to know that current test properties from square sections are not more benign than those experienced in plates and shells. Projects should incorporate a plan to test a statistical sample size of both configurations to provide the designer with an appropriate data base.

Bending Stresses: In-plane loading is the preferred strength application of butt-welds, but these same loads can induce bending when welds are designed into regions with abrupt geometric changes. This principle is especially appreciated in girth welds of pressure vessels where abrupt changes in meridional curvatures between end-closures and cylinders cause abrupt displacement differential at the intersection. Displacements are matched through shears and moments which induce local discontinuity stress waves that damp out over a length related to $(R\ t)^n$. In particular, local bending causes materials with the lowest elastic limit to hinge and assume a disproportionate share of distortion. The combination of the peak stress waves falling in the girth weld having the lowest elastic limit causes the weld material to yield first and progressively distort most.

Because bending displacement to failure is a function of weld width noted by equations (74) and (75), the wider the weld or the HAZ, the greater the safety margin. But controlling this geometric parameter is not a reliable method for designing high performance structures. Consequently, good design practices suggest that all welds be designed away from discontinuities wherever possible.

If local bending cannot be designed out of butt-welded plates, then the weld width determined by manufacturing process discretions must be analyzed to assure sustenance of the superimposed local moment displacements to within the specified margin; if it cannot, the plate thickness should be increased. Nevertheless, the final decision on weld width should invariable continue to rest with metallurgists and manufacturing considerations.

VI. STRAIN GAUGE DATA ANALYSIS

Strain gauge data analysis closes the loop on the structural modeling process. Structural failure predictions are based on four critical design uncertainties; maximum expected operating load analysis, manufacturing and processing quality and tolerances, strength of material confidence, and stress modeling assumptions and techniques. Only the last three combined uncertainties are verifiable from development structural test through strain response measurements on a test article under well-defined applied loads. Preferred measuring instruments are electrical strain gauges.

The primary purpose for applying the multitude of gauges that often move project managers is to assess the structural behavior of critical regions, to correlate measurements with the stress model predictions, and to ultimately fine-tune the prediction model. The calibrated model is then used to extract and verify loads, again through strain gauge data under actual operational environments. At this point, the uncertainties are not only resolved, but the verified model is used to determine safety margins with a variety of projected operational loads.

Another important application of strain gauge data correlation with prediction models is the verification of prototype safety factors. Because prototype test structures must remain operational after test, a maximum test load of 20 percent above the elastic limit is allowed. In this 20-percent nonlinear response sample, the strain gauge data is tracked with the nonlinear prediction model. If the gauge data and model predictions correlate very well, then the prototype article is expected to support the predicted ultimate safety factor.

In all the above cases, strain gauge data evaluation is a direct feedback to modeling predictions. To begin, strain gauge types, ranges, locations, and orientations are determined from a map of critical stress regions based on prediction models. The same map is required for evaluating the resulting test strain gauge data. Recorded strains are converted to the conventional domain of stresses used specifically in prediction and materials data bases. The conversion of multiaxial strain to inelastic stress variables is made difficult because the Poisson's ratio increases with stress, which in turn is nonlinearly related to stress. A conversion method follows which is based on the preceding analytical approach.

Stresses normal to a plate, or shell, are considered negligible so that a plain stress condition may be assumed to exist, $\sigma_y = 0$. The related principal stresses are similar to those derived in equation (60), and rewritten with orthotropic Poisson's ratios,

$$\sigma_x = a\left[\frac{\varepsilon_x + \mu_z\varepsilon_z}{(1 - \mu_x^2)}\right]^b , \tag{109}$$

$$\sigma_z = \frac{\sigma_x(\varepsilon_z + \mu_x\varepsilon_x)}{\varepsilon_x + \mu_z\varepsilon_z} . \tag{110}$$

Poisson's ratios are related to strain about each axis by equation (5),

$$\mu_x = g\,\varepsilon_x^f , \qquad \mu_z = g\,\varepsilon_z^f . \tag{111}$$

Substituting equation (111) into equations (109) and (110) produces the required principal stress equations expressed in measured strains,

$$\sigma_x = a\left[\frac{\varepsilon_x + g\varepsilon_z^{(1+f)}}{1 - g\varepsilon_x^{2f}}\right]^b , \tag{112}$$

$$\sigma_z = \sigma_x\left[\frac{\varepsilon_z + g\varepsilon_x^{(1+f)}}{\varepsilon_x + g\varepsilon_z^{(1+f)}}\right] .$$

38

Solving for the dominant stress, σ_x, from the first part of equation (112) and substituting into the second equation provides the two principal normal stresses.

Note that Poisson's ratio in the denominator of equations (109) is related to dominant strain, ε_x, as suggested in section II-F, though it is shared by strains ε_x and ε_z. The maximum error caused by this simplification may be determined from the nonlinear expression of Poisson's ratio in the first of equations (112). Differentiating stress σ_x with respect to ε_x in the denominator and dividing by the stress and strain gives the percent error of stress with percent change in strain,

$$\frac{d\sigma_x}{\sigma_x} = \frac{200 bfg\varepsilon_x^{2f}}{1 - g\varepsilon_x^{2f}} \frac{d\varepsilon_x}{\varepsilon_x} ,$$ (113)

where the maximum $d\varepsilon_x/\varepsilon_x = (\varepsilon_x - \varepsilon_z)/\varepsilon_x$.

Equation (112) is suitable only when axes of principal stresses on the test article are known and if shear stresses are not existent. A set of perpendicular strain gauges, tee rosettes, are used to measure these principal strains. Symmetrical pressure bottles and shells of revolution are examples of zero shear presence; but regions on plate or shell known to have inplane shear stresses must be instrumented with rectangular rosettes, figure 17, to obtain the third equation for solving three inplane strains.
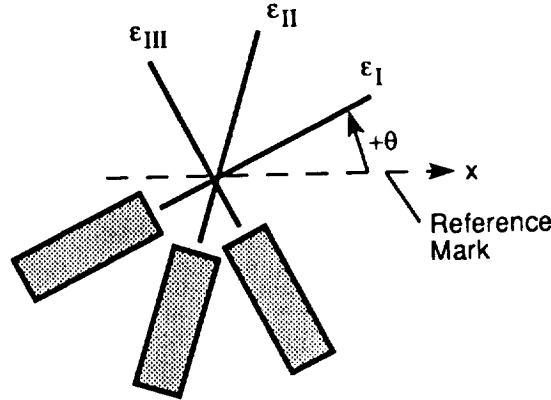
Figure 17. Rectangular rosette orientation.

The rectangular rosette has two perpendicular strain gauges with a third bisecting them at 45 degrees. They are mounted at some known angle with respect to a reference x-axis marked on the test article as shown. The relationship between strain gauge readings and the normal and shear strains is defined by the transformation matrix,

$$\begin{Bmatrix} \varepsilon_I \\ \varepsilon_{II} \\ \varepsilon_{III} \end{Bmatrix} = \begin{bmatrix} \cos^2(\theta) & \sin^2(\theta) & \sin(\theta)\cos(\theta) \\ \cos^2(\theta+45) & \sin^2(\theta+45) & \sin(\theta+45)\cos(\theta+45) \\ \cos^2(\theta+90) & \sin^2(\theta+90) & \sin(\theta+90)\cos(\theta+90) \end{bmatrix} \begin{Bmatrix} \varepsilon_x \\ \varepsilon_y \\ \gamma_{xy} \end{Bmatrix}$$ (114)

where the Roman numeral subscripts refer to the measured strains. Equation (114) has the form

$$X = [A] \, Y \ ,$$

from which the reference axis strains are resolved through its inverse matrix form,

$$Y = [A]^{-1} \, X \ .$$
(115)

Restating results of the stress tensor in section II with strains and substituting the strains resolved from equation (115) provide the principal strains at the rosette location

$$\varepsilon_{1,2} = \frac{\varepsilon_x + \varepsilon_z}{2} \pm \frac{1}{2} \sqrt{\varepsilon_x^2 + \varepsilon_z^2 - 2\varepsilon_x\varepsilon_z + \gamma_{xz}^2} \ .$$
(116)

The angle producing principal strains is

$$\tan 2\theta_p = \frac{\gamma_{xz}}{\varepsilon_x - \varepsilon_z} \ ,$$
(117)

and the maximum shear strain is

$$\gamma_{max} = \pm \frac{1}{2} \sqrt{\varepsilon_x^2 + \varepsilon_z^2 - 2\varepsilon_x\varepsilon_z + \gamma_{xz}^2} \ .$$
(118)

To convert principal strains to principal stresses, substitute results from equation (116) into equation (112) as before.

VII. MODELING VERIFICATION

A. Materials

There is adequate documentation on normal stress-strain data through the inelastic regime, but none on Poisson's ratio and shear strain at ultimate stress to verify models in section II. Orthotropic Poisson's ratios may be backed out of biaxial strain responses from known stresses developed on pressurized elliptical domes. This same test could verify strain gauge conversion equations (112).

Another task would be to verify the materials discontinuity stress phenomenon. A simple approach would be to test welded plate specimens having a width seven times the thickness to failure and compare the strength results with current weld specimen having square test sections. A more comprehensive task would incorporate a photoelastic coat to assess plastic strain variations associated with HAZ, fillet, and base properties concurrently in the weld region.

B. Analytical Models

Though analytical model developments were based on logical extensions of sound physical principles, some simplifications were necessary to reduce certain models to practical forms. Except for the materials discontinuity stress development, a necessary mathematical check for all inelastic models was to substitute the linear parameters $a = E$ and $b = 1$ to assure these expressions collapsed to the familiar textbook strength of materials formulas. It should be interesting to experimentally verify the plate bending model.

Since SRB skirt ultimate safety factor prediction by the NASTRAN code was similar to the ANSYS code, using both plastic options and brick elements, it would seem appropriate to also suspect NASTRAN plate results until verified by a similar ANSYS task [6].

VIII. SUMMARY

The safety of all structures depends upon the inelastic strength to ultimate stress behavior, yet this phenomenon is not well known. Perhaps there has been little incentive to dwell into intellectual nonlinear analyses that are bumped against arbitrary safety factors when a structural test to failure can more positively confirm the ultimate safety margin. However, it does not provide the physics of failure. When a critical high performance structure failed short of predictions and a redesign again failed short with no further clues as to the mechanics of failure, it became necessary to understand the structural behavior of inelastic stress as applied to design through test analysis.

The behavior of structures beyond the elastic limit is typical of the elastic-plastic mechanics of appendix C, which is neither very versatile nor comprehensible to the prevalent designer. Instead, the approach employed was an analytical method similar to the piece-wise linear technique used with linear computational codes and stepped nonlinear material inputs. The analytical method difference is that nonlinear material properties were expressed in engineering stresses and strains and modeled in exponential form, and were then integrated with strength of materials linear stress and strain expressions. The integration of these exponential expressions is continuous which allows for fine focused solutions.

Several analytical structural models were developed that are basic to plate and shell welded construction, and predictions were compared with a commercial FEM. A common strain error characteristic to all FEM bending models was noted. Computed maximum bending strains of FEM codes are not at the surface, but they are predictions at the centroid of the surface element, figure 17, resulting in a lower strain prediction.

A simple plate structure was modeled with the same ANSYS code using the same SRB skirt plastic material and brick options. The uniaxial specimen produced mixed results. Axial strain predictions were low enough to imply an inappropriate lateral constraint, but the strain ratios did not comply with nor without that constraint. Bending specimen results did not conform to plate continuity conditions in which the lateral strain along the width must equal zero. In comparing the net results of the ANSYS plate compliance and surface error predictions with the analytical method, the ANSYS method rendered 50 percent less strain.

Based on the few SRB related examples, the ANSYS plastic brick option was clearly not an appropriate model for the aft skirt stress analysis beyond the elastic limit. Since the NASTRAN code predictions, using similar options, fell just as short as the ANSYS, the NASTRAN method should be suspect until scrutinized similarly to the ANSYS task [6]. Inelastic analysis may still be accomplished with either code by incorporating nonlinear material properties into the linear elastic option in the familiar step-wise fashion. This step-wise method is recommended as a back-up approach for future design analysis.

Discovery of weld discontinuity stresses was reported earlier [1] and was incorporated into the analytical method developed in this study for completeness. Results indicate shear stress is a significant factor in the failure criteria, which has a very narrow distribution, and peaks 2 percent below the plate surface at the material discontinuity interface. It is not possible to experimentally detect it, and it is difficult to model it through FEM. Combined discontinuity stresses are not dependent on geometry, but are strongly dependent on the relative properties of the interfacing elements; first on the ratio of their elastic limit stresses, and then on the strain hardening exponent ratios. The implication is that material discontinuity stress may occur in a very narrow band of the weakest material.

The exact stress and strain coupling under combined tension and bending loads was resolved through the analytical method with some rather surprising behavior, figure 10. When measured strains from back-to-back gauge exceed the elastic limit, the bending strain may be several times larger than the axial strain, but the stress is a small fraction of the axial stress. This model provides the basis for assessing operational loads sensitivities. Because it is an often encountered condition and lengthy to solve, it was programmed and included in appendix A.

Another surprise was the tee rosettes strain gauge conversion to stress expressions. While one of the stress formulas was similar to the elastic conversion, the second, equation (110), was distinctly different. In substituting elastic properties into equations (109) and (110), both equations collapse to the familiar elastic conversion formulas.

Analytical models presented are related to the skirt failure, other models may be similarly derived as required. What began as a troubleshooting task evolved into an analytical technique waiting to happen. To understand the inelastic behavior of specific structures, existing nonlinear material models were modified to combine with existing strength models. As more models were derived, a common technique emerged that was extendable to combined and multiaxial loading. When the technique was not only applicable, but required, to convert strains from test data to stresses, the analytical loop was complete. There are limits to its application, as there are to plasticity theory, but the technique is another option friendly to a larger spectrum of analysts.

REFERENCES

1. Verderaime, V.: "Weld Stresses Beyond Elastic Limit, Material Discontinuity." NASA TP 2935, August 1989.

2. Bianca, C.J.: Presentation on "Use of Safety Factor of 2.0 for No-Test Option," January 24, 1990.

3. MIL-Handbook C5, "Metallic Materials and Elements for Aerospace Vehicle Structures," September 1976.

4. Vaughn, T.P.: MSFC Metallic Materials Division Project 86-020-EH23, report to be published.

5. Freudenthal, A.M.: "The Inelastic Behavior of Engineering Materials and Structures." John Wiley and Sons, 1950.

6. Berry, D.M.: "Aft Skirt Analysis." Vol. I, Contract NAS8-37282, April 1989.

7. Timoshenko and Gere: "Theory of Plates and Shells." McGraw-Hill, second edition.

8. Flügge, W.: "Handbook of Engineering Mechanics." McGraw-Hill, 1962.

APPENDIX A

NEWTON-RAPHSON METHOD

1. Combined Stresses, Bar Specimen

Two unknown variables, C and ε_M, are implicit in the two equations (55) and (56). These variables may be determined through the Newton-Raphson method by rearranging both equations in the following functional form.

$$F1 = \frac{a(h-C)}{\varepsilon_M(b+1)} |\psi 1 - \psi 2| - N \ . \tag{A-1}$$

$$F2 = \frac{a(h-C)}{(b+1)\varepsilon_M}\left\{\psi 2\left[h+\frac{(h-C)}{(b+2)}\left[\frac{\varepsilon_N}{\varepsilon_M}-\frac{(h+C)}{(h-C)}\right]\right] + \psi 1\left[h-\frac{(h-C)}{(b+2)}\left[\frac{\varepsilon_N}{\varepsilon_M}+1\right]\right]\right\} - M \tag{A-2}$$

and estimating starting values for these unknowns. Then,

$$F_{10}+\left[\frac{\partial F_1}{\partial \varepsilon_M}\right]\Delta\varepsilon_M+\left[\frac{\partial F_1}{\partial C}\right]\Delta C = 0 \ , \quad \text{and} \quad F_{20}+\left[\frac{\partial F_2}{\partial \varepsilon_M}\right]\Delta\varepsilon_M+\left[\frac{\partial F_2}{\partial C}\right]\Delta C = 0 \ , \tag{A-3}$$

where

$$\Delta\varepsilon_{M1} = \varepsilon_{M1} - \varepsilon_{M0} \ , \quad \text{and} \quad \Delta C = C_1 - C_0 \ . \tag{A-4}$$

Let:

$$G_1 = \frac{\partial F_1}{\partial \varepsilon_M} \ , \quad G_2 = \frac{\partial F_2}{\partial \varepsilon_M}$$

$$L_1 = \frac{\partial F_1}{\partial C} \ , \quad L_2 = \frac{\partial F_2}{\partial C}$$

$$Y_1 = F_{10} \ , \quad Y_2 = F_{20} \ . \tag{A-5}$$

then

$$G_1 \Delta\varepsilon_M+L_1\Delta C = -Y_1$$

$$G_2 \Delta\varepsilon_M+L_2\Delta C = -Y_2 \ . \tag{A-6}$$

and

$$K = \begin{vmatrix} G_1 & L_1 \\ G_2 & L_2 \end{vmatrix} \qquad K_1 = \begin{vmatrix} Y_1 & L_1 \\ Y_2 & L_2 \end{vmatrix} \qquad K_2 = \begin{vmatrix} G_1 & Y_1 \\ G_2 & Y_2 \end{vmatrix} . \qquad \text{(A-7)}$$

Resulting variables,

$$\varepsilon_{M1} = \varepsilon_{M0} - \frac{K_1}{K}, \quad \text{and} \quad C_1 = C_0 - \frac{K_2}{K}, \qquad \text{(A-8)}$$

are iterated to desired tolerance,

$$ABS \left| \frac{\varepsilon_{M0} - \varepsilon_M}{\varepsilon_{M0}} \right| \leq \text{Tol}. \qquad \text{(A-9)}$$

' PROGRAM, COMBINED PLASTIC AXIAL-BENDING LOADS (BAR SPECIMEN)
' moment must be greater than zero

```
' INPUTS
M=7.5                        'external applied moment, kip-in/in
P=40                         '          "          axial load, kips/in
H=.72                        ' plate half-thickness
A=98                         'strength coeff. of mat'l
B=.22
BB=B+1                       'hardening exponent of mat'l
PH= P/(2*H*A)
EP=(ABS(PH))^(1/B)           'strain caused by axial load

'estimate unknown variables
INPUT "estimate EM=";EM      'strain caused by moment
INPUT "estimate C=";C        'bending neutral axis from y=0, inch.   0<= -C<-H

' NEWTON-RAPHSON METHOD
J=0
START: Q1=EM*.0011: Q2=C*.0011
  CALL FUNCTION(M,P,H,A,B,BB,EP,EM,C,F1,F2)
D1=EM: D2=C: Y1=F1: Y2=F2: EM=EM+Q1
  CALL FUNCTION(M,P,H,A,B,BB,EP,EM,C,F1,F2)
G1=(F1-Y1)/Q1: G2=(F2-Y2)/Q1: C=C+Q2: EM=D1
  CALL FUNCTION(M,P,H,A,B,BB,EP,EM,C,F1,F2)
L1=(F1-Y1)/Q2: L2=(F2-Y2)/Q2

'cramer's rule
K=G1*L2-G2*L1
K1=Y1*L2-Y2*L1
K2=G1*Y2-G2*Y1
EM=D1-K1/K
C=D2-K2/K
J=J+1
```

46

```
PRINT "EM=",EM," C=",C
IF ABS((D1-EM)/D1)>.000001 GOTO START

'AXIAL- BEND PROFILE
OPEN"CLIP:" FOR OUTPUT AS #3

YS=H: YF=-H: NY=25
N=NY-1
DY=(YF-YS)/N
  ET=0: ST=0 .
  Y=YS
  FOR I=1 TO N
  ET=EP+(Y-C)*EM/(H-C)            'ET= combined strain
  ST=A*((ABS(ET))^B)*SGN(ET)      'ST= combined stress
  SP=P/(2*H)                      'SP = AXIAL STRESS

WRITE #3,Y,ET,ST,EP,SP
PRINT Y, ET,ST,EP,SP
  Y=YS+(I+1)*DY
  NEXT I

CLOSE #3
STOP

SUB FUNCTION (M,P,H,A,B,BB,EP,EM,C,F1,F2) STATIC

R1=A*(H-C)/EM/BB
R2=EP+EM
R3=EP-EM*(H+C)/(H-C)
R4=((ABS(R2))^BB)
R5=((ABS(R3))^BB)
R6=H+((H-C)/(B+2))*(EP/EM-(H+C)/(H-C))
R7=H-((H-C)/(B+2))*(EP/EM+1)

F1 =R1*(R4-R5)-P
F2 =R1*(R4*R7+R5*R6)-M

PRINT EM, C

END SUB
```

2. Combined Stresses, Plate Specimen

The two unknown variables, C and ε_M, implicit in equations (80) and (81) may be solved by the Newton-Raphson method. Rearranging both equations in the functional form as before,

$$F3 = \frac{(h-C)[\psi3 - \psi4]}{(\beta+1)\varepsilon_M}\left[\frac{a^{1/b}}{Q}\right]^{\beta} - N \ , \tag{A-10}$$

$$F4 = \frac{(h-C)}{(\beta+1)\varepsilon_M}\left[\frac{a^{1/b}}{Q}\right]^{\beta}\left\{\psi4\left[h+\frac{(h-C)}{(\beta+2)}\left[\frac{\varepsilon_N}{\varepsilon_M}-\frac{(h+C)}{(h-C)}\right]\right] + \psi3\left[h-\frac{(h-C)}{(\beta+2)}\left[\frac{\varepsilon_N}{\varepsilon_M}+1\right]\right]\right\} - M \tag{A-11}$$

proceed with equations (A-3) through (A-9) above. A program used in section IV in this document follows.

```
' INPUTS
M=10                                    'external applied moment, kip-in/in
P=40                                    '         "       axial load, kips/in

H=.72                                   ' plate half-thickness
SU=45.7                                 'max stress, ksi
SE=26.3                                 'elastic limit stress, ksi
EU=.04                                  'max strain
E=10500                                 'Young's modulus, ksi
B=LOG(SU/SE)/LOG(EU*E/SE)               'hardening exponent of mat'l
A=SE/((SE/E)^B)                         'strength coeff. of mat'l
BE=1/B

SP= P/(2*H)                             'applied axial stress, ksi

'Poisson's ratio
UUA=((SE/A)^BE)*E/SE
UA=.5*UUA+.3*(1-UUA)
'U=.5-(UA-.3)*S/E*((A/S)^BE)            'poisson's ratio at any stress s

'plate coefficient
UXEL=.5-(UA-.3)*SE/E*((A/SE)^BE)        'poisson ratio at elastic limit
UXU=.5-(UA-.3)*SU/E*((A/SU)^BE)         'poisson ratio at ultimate
GAEL=1-UXEL^2                              'plate coef at elastic limit
GAU=1-UXU^2                                'plate coef at ultimate
R=LOG(GAU/GAEL)/LOG(SU/SE)
Q=GAEL/(SE^R)
BP=B/(1+B*R)                            'plate combined expo.

EP=(SP/A)^BE                            'strain caused by axial load

'estimate unknown variables
INPUT "estimate EM=";EM                 'strain caused by moment
INPUT "estimate C=";C                   'bending neutral axis from y=0, inch.  0<= -C<-H

' NEWTON-RAPHSON METHOD
J=0
START: Q1=EM*.0011: Q2=C*.0011
  CALL FUNCTION(M,P,H,A,B,BE,EP,EM,C,BP,Q,F1,F2)
D1=EM: D2=C: Y1=F1: Y2=F2: EM=EM+Q1
  CALL FUNCTION(M,P,H,A,B,BE,EP,EM,C,BP,Q,F1,F2)
G1=(F1-Y1)/Q1: G2=(F2-Y2)/Q1: C=C+Q2: EM=D1
  CALL FUNCTION(M,P,H,A,B,BE,EP,EM,C,BP,Q,F1,F2)
L1=(F1-Y1)/Q2: L2=(F2-Y2)/Q2

'cramer's rule
K=G1*L2-G2*L1
K1=Y1*L2-Y2*L1
K2=G1*Y2-G2*Y1
EM=D1-K1/K
C=D2-K2/K
J=J+1

PRINT "EM=",EM," C=",C
IF ABS((D1-EM)/D1)>.000001 GOTO START

'AXIAL- BEND PROFILE
OPEN"CLIP:" FOR OUTPUT AS #3
```

48

```
YS=H: YF=-H: NY=25
N=NY-1
DY=(YF-YS)/N

ET=0: ST=0
Y=YS
FOR I=1 TO N
ET= EP+(Y-C)*EM/(H-C)                              'total strain vs thickness
  ST=(((A^BE)/Q)^BP)*((ABS(ET))^BP)*SGN(ET)   'total stress vs thickness


WRITE #3,Y,ET,ST,EP,SP
PRINT Y, ET,ST,EP,SP
  Y=YS+(I+1)*DY
  NEXT I

CLOSE #3

STOP

SUB FUNCTION (M,P,H,A,B,BE,EP,EM,C,BP,Q,F1,F2) STATIC
R1=(((A^BE)/Q)^BP)*(H-C)/EM/(BP+1)
R2=EP+EM
R3=EP-EM*(H+C)/(H-C)
R4=((ABS(R2))^(BP+1))
R5=((ABS(R3))^(BP+1))
R6=H+((H-C)/(BP+2))*(EP/EM-(H+C)/(H-C))
R7=H-((H-C)/(BP+2))*(EP/EM+1)

F1 =R1*(R4-R5)-P
F2 =R1*(R4*R7+R5*R6)-M

PRINT EM, C

END SUB
```

APPENDIX B

DISCONTINUITY STRESS MODEL

A model is required for determining local stress components on a fillet weld specimen caused by an abrupt change in lateral displacement at the bonded interface. Induced inplane shear stresses. τ_{xy}. should be zero at the top and bottom surfaces and at the midthickness, and the lateral normal stress. σ_y. should be zero at both surfaces. These boundary conditions may be satisfied by inventing a dummy interfacing element having the same thickness as the fillet and subjecting it to a uniform external load. q. over a suitable length. d. The load. q. induces a uniform lateral strain. ε_y. across the thickness except at the interface. where the stresses and displacements are matched with the fillet element.

Since the dummy element is used only to simulate boundary conditions at the weld bond. stress distributions for $x < d$ are not relevant to the problem. Therefore. the lateral loading. q. and axial loading. σ_x. will be related to the common interface displacement to eliminate the lateral load from the discontinuity stress analysis in section V. It follows that the origin of the x-axis will be shifted in the text from the position shown in figure B-1 to a point on the interface.
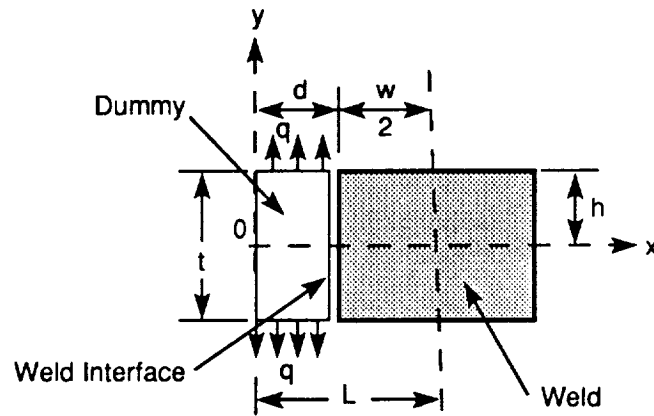

Figure B-1. Weld interface model.

Figure B-1 describes a simply connected contour with inplane forces which makes it independent of material constants. The geometry and the discontinuous dummy loading q are symmetrical about the x- and y-axes. This is a classical problem [8] applicable to the generalized plane stress method. It consists of integrating the compatibility equation.

$$\frac{\partial^4\Phi}{\partial x^4} + 2\frac{\partial^4\Phi}{\partial x^2\partial y^2} + \frac{\partial^4\Phi}{\partial y^4} = 0 , \tag{B-1}$$

where Airy's stress function. Φ. is defined by three components derived from equilibrium:

$$\sigma_x = \frac{\partial^2\Phi}{\partial y^2} , \quad \sigma_y = \frac{\partial^2\Phi}{\partial x^2} , \quad \sigma_{xy} = \frac{\partial^2\Phi}{\partial x\partial y} . \tag{B-2}$$

51

Equation (B-1) is of the form $\Phi(x,y) = XY$ whose solution is well known to be

$$\Phi(x,y) = (C_1 \cos \lambda x + C_2 \sin \lambda x)(C_3 \cosh \lambda y + C_4 \sinh \lambda y + C_5 y \cosh \lambda y + C_6 y \sinh \lambda y) \quad (B-3)$$

where $C_1,...C_6$ are arbitrary constants and $\lambda = m\pi/L$ for $m = 1,2,...$ Substituting equation (B-3) into (B-2), satisfying stress boundary conditions

$$\tau_{xy} = -\frac{\partial^2 \Phi}{\partial x \partial y} = 0 \quad \text{at } x = \pm h \text{ and } y = \pm L ,$$

and allowing that $\sin \lambda x$ to vanish for a symmetrical loading of

$$Q = A + \sum_1^n B \cos \frac{\Pi m x}{L} , \qquad (B-4)$$

at $y = \pm h$, determined the constants to be

$$C_1 = 1 \quad \text{and} \quad C_2 = C_4 = C_5 = 0 .$$

Stress components of equation (2) become:

$$\sigma_x = \frac{\partial^2 \phi}{\partial y^2} = 2Q \sum \frac{\cos \lambda x}{2\lambda h + \sinh 2\lambda h}[(\lambda h \cosh \lambda h - \sinh \lambda h) \cosh \lambda y - (\sinh \lambda h) \lambda y \sinh \lambda y] ,$$

$$\sigma_y = \frac{\partial^2 \phi}{\partial x^2} = 2Q \sum \frac{\cos \lambda x}{2\lambda h + \sinh 2\lambda h}[(\sinh \lambda h) \lambda y \sinh \lambda y - (\lambda h \cosh \lambda h + \sinh \lambda h) \cosh \lambda y] ,$$

$$\tau_{xy} = -\frac{\partial^2 \Phi}{\partial x \partial y} = 2Q \sum \frac{\sin \lambda x}{2\lambda h + \sinh 2\lambda h}[(\lambda h \cosh \lambda h) \sinh \lambda y - (\sinh \lambda h) \lambda y \cosh \lambda y]. \qquad (B-5)$$

Dummy uniform tension loading terms, A and B, of equation (B-4) are found in the usual way:

$$\int_{-L}^{L} A \, dx = \int_{-d}^{d} q \, dx ,$$

where $A = qd/L$, and

$$B = \frac{2}{L} \int_0^d q \cos \lambda x \, dx + \int_d^L (0) = \frac{2q}{\lambda L} \sin \lambda d . \qquad (B-6)$$

Evaluating A for integers $0 < m < 1$ in each stress component as λ approaches zero for $y = 0$, A becomes zero for σ_x and τ_{xy}, and $A/2$ for σ_y. Let $m\pi = \alpha$ and

$$\lambda d = \alpha d/L = \alpha T , \quad \lambda x = \alpha x/L = \alpha X , \quad \lambda h = \alpha h/L = \alpha H , \quad \lambda y = \alpha y/L = \alpha Y . \quad \text{(B-7)}$$

Substituting the evaluated A, equation (B-6), and identities (B-7) into (B-5) gives the discontinuity stress factors in nondimensional form,

$$\frac{\sigma_x}{q} = 4\sum \frac{\sin \alpha T \cos \alpha X}{(2\alpha H + \sinh 2\alpha H)\,\alpha} \left[(\alpha H \cosh \alpha H - \sinh \alpha H) \cosh \alpha Y - (\sinh \alpha H)\,\alpha Y \sinh \alpha Y\right]$$

$$\frac{\sigma_y}{q} = T + 4\sum \frac{\sin \alpha T \cos \alpha X}{(2\alpha H + \sinh 2\alpha H)\,\alpha} \left[(\sinh \alpha H)\,\alpha Y \sinh \alpha Y - (\alpha H \cosh \alpha H + \sinh \alpha H) \cosh \alpha Y\right]$$

$$\frac{\tau_{xy}}{q} = 4\sum \frac{\sin \alpha T \sin \alpha X}{(2\alpha H + \sinh 2\alpha H)\,\alpha} \left[(\alpha H \cosh \alpha H) \sinh \alpha Y - (\sinh \alpha H)\,\alpha Y \cosh \alpha Y\right] .$$

(B-8)

Discontinuity stress factors distribution over the length and half thickness are calculated from equations (B-8) and plotted in figure B-2 for $m = 4$ which was limited by program overflow. Discontinuity stress factors distribution at the bond interface are determined from equation (B-8) by letting $\alpha X = \alpha T$. Recognizing that αH is large so that $\sinh \alpha H = \cosh \alpha H$, and $2\alpha H$ is small, discontinuity stresses at the interface are

$$D_x = \frac{\sigma_x}{q} = 4\sum_1^m \sin \alpha T \cos \alpha T \, [e^{-\alpha H}] \left[\left(H - \frac{1}{\alpha}\right) \cosh \alpha Y - Y \sinh \alpha Y\right]$$

$$D_y = \frac{\sigma_y}{q} = T + 4\sum_1^m \sin \alpha T \cos \alpha T \, [e^{-\alpha H}] \left[Y \sinh \alpha Y - \left(H + \frac{1}{\alpha}\right) \cosh \alpha Y\right]$$

$$D_{xy} = \frac{\sigma_{xy}}{q} = 4\sum_1^m \sin \alpha T \sin \alpha T \, [e^{-\alpha H}][H \sinh \alpha Y - Y \cosh \alpha Y] . \quad \text{(B-9)}$$

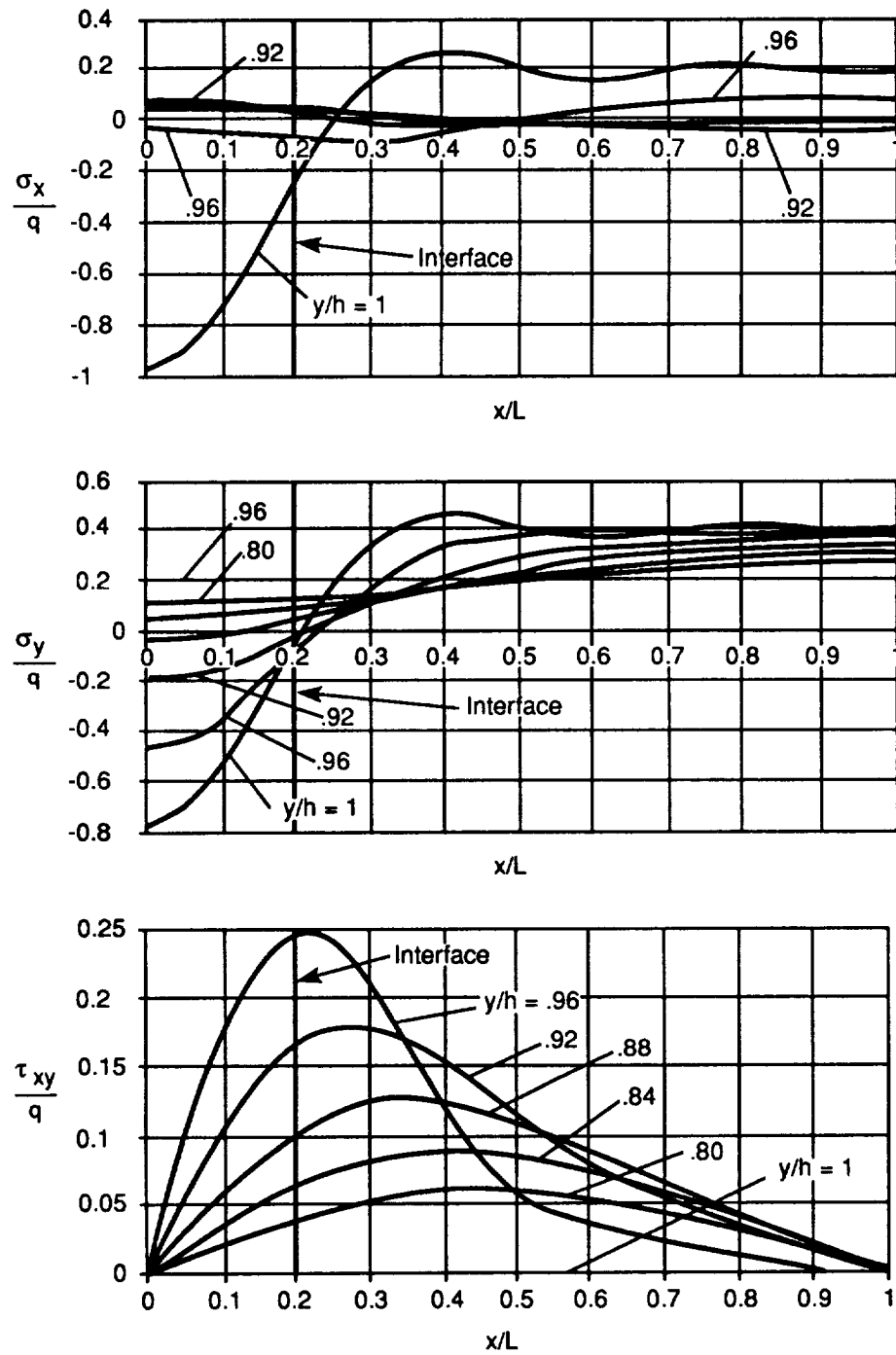Stress component factor distributions of equation (B-9) are plotted in figure B-3.

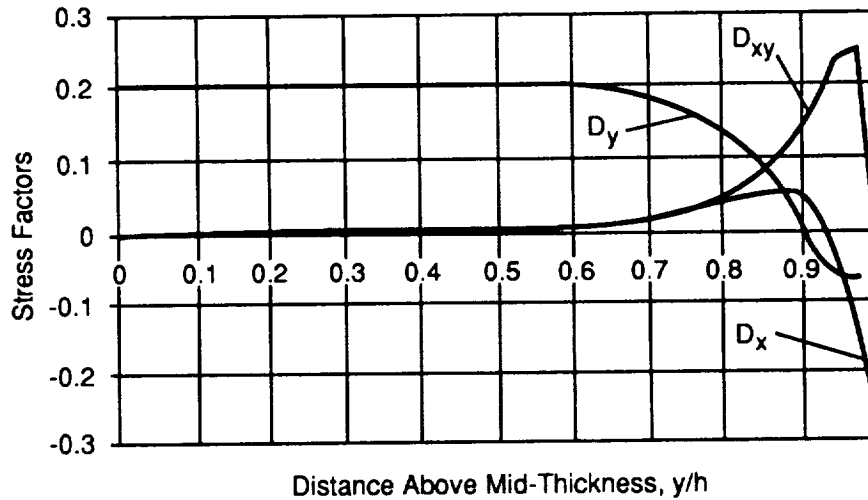Figure B-2. Discontinuity stress component factors.

Figure B-3. Stress factors distribution on bond interface.

PROGRAM MATERIAL DISCONTINUITY, FIGURE (16)
' STRESS FACTOR @ ULT STRESS DISTRIBUTION ALONG Y-AXIS INTERFACE

' H1=h/l, H2=d/l, Y1=y/l, X2=x/l, SXY=shear, SX=axial, SY=norm. t/w = H1/ (1-d)
OPEN "CLIP:" FOR OUTPUT AS #2

' geo input
H2= .2
H1=4.6
M1= 5

' material INPUTS
SU1=58   'max stress PLATE, ksi
SU2=48.6   '   DO WELD
SE1=32   'elastic limit stress PLATE, ksi
SE2=26.5   '   DO WELD
EU1=.04   'max PLATE strain
EU2=.04   ' DO WELD
E=10500   'Young's modulus, ksi
EE1=SE1/E   'elastic limit
EE2=SE2/E

' calculated material properties
B1=LOG(SU1/SE1)/LOG(EU1*E/SE1)   'hardening exponent of PLATE mat'l
A1=SE1/((SE1/E)^B1)   'strength coeff. of mat'l
B2=LOG(SU2/SE2)/LOG(EU2*E/SE2)   'hardening exponent of WELD mat'l
A2=SE2/((SE2/E)^B2)   'strength coeff. of mat'l

EK2=EU2/3
SK1=A1*EK2^B1
SK2=A2*EK2^B2

BB1=LOG((SU1-SE2)/(SK1-SE2))
BB1=BB1/LOG((EU1-EE2)/(EK2-EE2))
AA1=(SK1-SE2)/((EK2-EE2)^BB1)

```
BB2=LOG((SU2-SE2)/(SK2-SE2))
BB2=BB2/LOG((EU2-EE2)/(EK2-EE2))
AA2=(SK2-SE2)/((EK2-EE2)^BB2)

'poisson's ratio
UXU1=.5-.2*SU1/E*((A1/SU1)^(1/B1))        'poisson's ratio OF PLATE at ULT stress
UXEL1=.3
UXU2=.5-.2*SU2/E*((A2/SU2)^(1/B2))        'poisson's ratio OF WELD at ULT stress
UXEL2=.3
F1=LOG(UXU1/UXEL1)/LOG((SU1/SE1)^(1/B1))
G1=.3/((SE1/A1)^(F1/B1))
F2=LOG(UXU2/UXEL2)/LOG((SU2/SE2)^(1/B2))
G2=.3/((SE2/A2)^(F2/B2))

UXK=.3+(UXU2-UXEL2)/3
SKU1=A1*(UXK/G1)^(B1/F1)
SKU2=A2*(UXK/G2)^(B2/F2)

FF1=LOG((UXU1-UXEL2)/(UXK-UXEL2))
FF1=FF1/LOG((SU1-SE2)/(SKU1-SE2))
GG1=(UXK-UXEL2)/((SKU1-SE2)^FF1)

FF2=LOG((UXU2-UXEL2)/(UXK-UXEL2))
FF2=FF2/LOG((SU2-SE2)/(SKU2-SE2))
GG2=(UXK-UXEL2)/((SKU2-SE2)^FF2)

R1S=0: R1F=1! : NR1=41 : DR1=(R1F-R1S)/(NR1-1)        'Y=0 to 1
FOR I=1 TO NR1
     R1=R1S+(I-1)*DR1                           '   R!=Y/H
     Y1=R1*H1                              'y/L=%h/L
     GOSUB T2SUB

     WRITE #2,R1,T2(1),T2(2),T2(3),T2(4)
     PRINT R1;T2(1);T2(2);T2(3);T2(4)

NEXT I
     CLOSE #2

STOP

T2SUB:
     SX=0
     SY=0
     SXY=0
     SK=0
      FOR M=1 TO M1
      A=M*3.1416
      AH2=A*H2
      AX2=AH2
      AH1=A*H1
      AY1=A*Y1

      EY1=EXP(AY1)
      EYN1=EXP(-AY1)
      SHY1=(EY1-EYN1)*.5
      CHY1=(EY1+EYN1)*.5
      EH1=EXP(AH1)
      EH1N=EXP(-AH1)
```

56

```
      SHH1=(EH1-EH1N)*.5
      CHH1=(EH1+EH1N)*.5
      E2H=EXP(2*AH1)
      E2HN=EXP(-2*AH1)
      SH2H1=(E2H-E2HN)*.5

      C1=SIN(AH2)*EH1N

      CX=(H1-1/A)*CHY1-Y1*SHY1
      CX=CX*C1*COS(AX2)
      SX=SX+CX

      CY=Y1*SHY1-(H1+1/A)*CHY1
      CY=CY*C1*COS(AX2)
      SY=SY+CY

      CXY=H1*SHY1-Y1*CHY1
      CXY=CXY*C1*SIN(AX2)
      SXY=SXY+CXY

      CK=H1*CHH1-(H1+2/A)*SHH1
      CK=CK*C1*COS(AX2)/AH1
      SK=SK+CK

      NEXT M

K2=1/(H2+4*SK)                                    'EQUATION V-16
Q1=1-(GG1*(AA2^(1/BB2)))/(GG2*(AA1^(1/BB1)))
Q1=Q1*K2*GG2/(AA2^(1/BB2))
Q1=Q1/(1+(A2^(1/B2))/(A1^(1/B1)))
K3=A2*Q1^B2                                       'EQUATION V-19

      SSX=4*SX*K3
      SSY=(H2+4*SY)*K3
      SSXY=4*SXY*K3

      K4=(FF2*BB2+1)*B2/BB2
      K5=((SU2-SE2)^K4)/SU2

      T2(1)=SSX*K5                      'equs V-22
      T2(2)=SSY*K5
      T2(3)=SSXY*K5
      T2(4)=(1+(T2(1))^2+T2(2)^2-(1+T2(1))*T2(2)+3*T2(3)^2)^.5        'equ V-23

RETURN
END
```

.

APPENDIX C

MATERIALS ANALOG

There are three noble disciplines from which mechanical behavior of most materials may be modeled: elasticity, viscosity, and plasticity. Their responses are unique to their content of force, displacement, and time variables. These three basic disciplines may be combined (fig. C-1) to further define mechanical behavior of more complicated, though common, engineering materials.

Viscoelasticity is emerging into a discipline of its own. It has borrowed from the large body of elasticity principles and coupled them with time-displacement behavior of fluids to represent polymer material behavior.

Bingham materials are represented by visco-plastic behavior. Most common of these materials are wet paints and printer's ink. Plastic-elastic behavior is inherent to most polycrystalline materials stressed beyond the elastic limit.
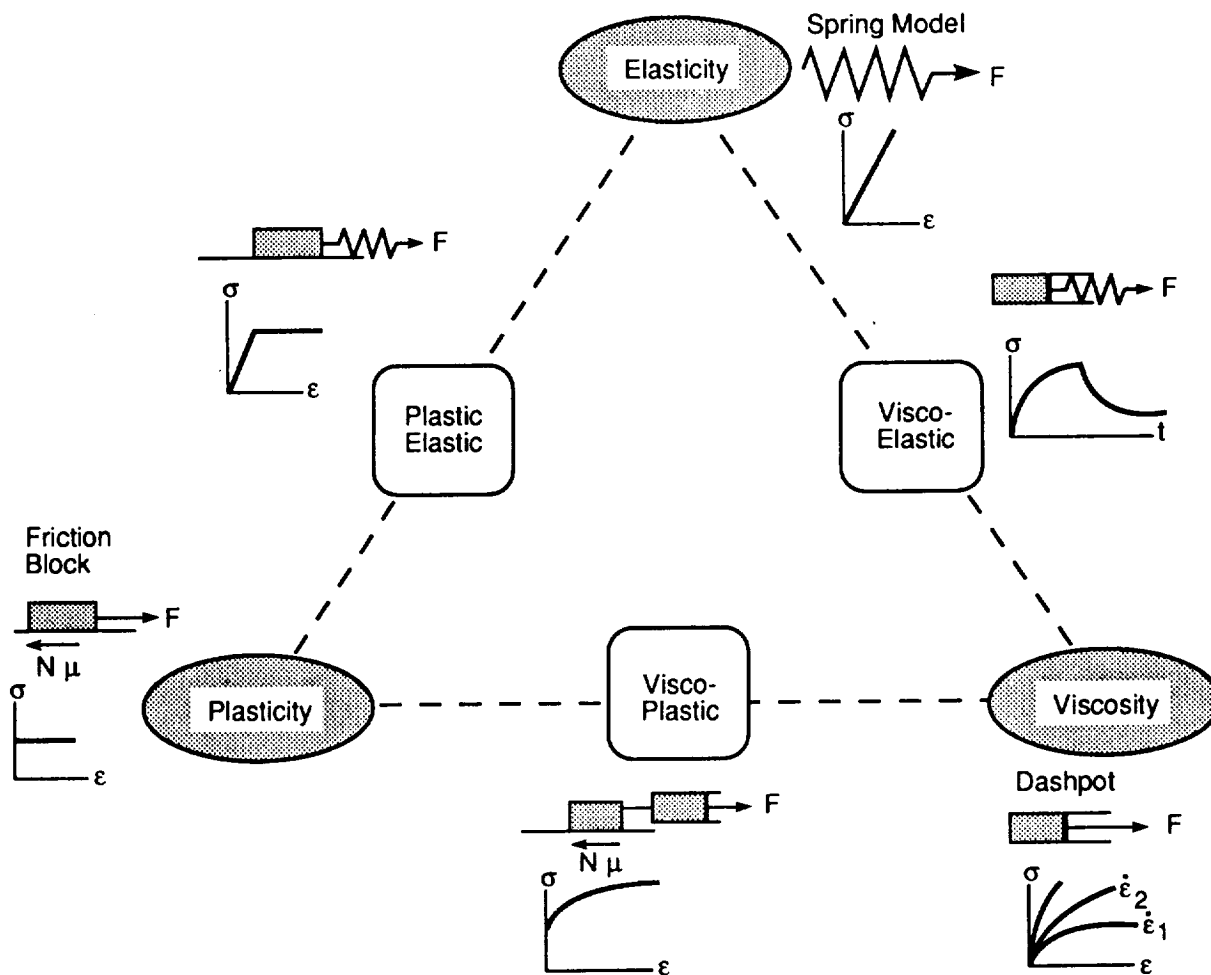
Figure C-1. Mechanical representation of common engineering materials.

Report Documentation Page

1. Report No. NASA TP-3075	2. Government Accession No.	3. Recipient's Catalog No.

4. Title and Subtitle Plate and Butt-Weld Stresses Beyond Elastic Limit, Material and Structural Modeling	5. Report Date **January 1991**
	6. Performing Organization Code

7. Author(s) V. Verderaime	8. Performing Organization Report No.
	10. Work Unit No. M-654

9. Performing Organization Name and Address George C. Marshall Space Flight Center Marshall Space Flight Center, Alabama 35812	11. Contract or Grant No.
	13. Type of Report and Period Covered Technical Paper

12. Sponsoring Agency Name and Address National Aeronautics and Space Administration Washington, DC 20546	14. Sponsoring Agency Code

15. Supplementary Notes

Prepared by Space Science Laboratory, Science and Engineering Directorate.

16. Abstract

Ultimate safety factors of high performance structures depend on stress behavior beyond the elastic limit—a region not too well understood. An analytical modeling approach was developed to gain fundamental insights into inelastic responses of simple structural elements. Nonlinear material properties were expressed in engineering stresses and strains variables and combined with strength of material stress and strain equations similar to numerical piece-wise linear method. Integrations are continuous which allows for more detailed solutions. Included with interesting results are the classical combined axial tension and bending load model and the strain gauge conversion to stress beyond the elastic limit. Material discontinuity stress factors in butt-welds were derived. This is a working-type document with analytical methods and results applicable to all industries of high reliability structures.

17. Key Words (Suggested by Author(s)) inelastic stress, weld stress, analytical modeling, inelastic modeling, FEM versus analytical, strain gauges, material discontinuity	18. Distribution Statement Unclassified – Unlimited Subject Category: 39

19. Security Classif. (of this report) Unclassified	20. Security Classif. (of this page) Unclassified	21. No. of pages 64	22. Price A04